Molybdenum and titanium isotopic signatures of arc-derived cumulates

Julian-Christopher Storck [a,*], Nicolas David Greber [a,b], Joana Filipa Vieira Duarte [a],
Pierre Lanari [a], Massimo Tiepolo [c], Thomas Pettke [a]

[a] *Institute of Geological Sciences, University of Bern, Baltzerstrasse 1+3, CH-3012 Bern, Switzerland*
[b] *Muséum d'histoire naturelle de Genève, Route de Malagnou 1, CH-1208 Genève, Switzerland*
[c] *Dipartimento di Scienze della Terra "A. Desio", Università degli Studi di Milano, Via Botticelli, 23 I-20133 Milano, Italy*

ARTICLE INFO

ABSTRACT

Fluid migration and/or differentiation of magmas in arc settings are important drivers of stable-isotope fractionation of elements like molybdenum and titanium, respectively. For both isotope systems, evolved magmas are heavier than average arc-basalts, which requires an isotopically light reservoir counterbalancing the heavy felsic lithologies.

In an attempt to better define this isotopically light reservoir, we investigate Mo and Ti isotopic signatures of upper crustal magmatic cumulates comprising hornblendites and gabbros from the Alpine orogen, the Sierra Nevada batholith, the Sanandaj-Sirjan zone and the Kos volcano-plutonic system. The cumulates and mafic enclaves exhibit Ti isotopic compositions ranging from that of arc-basalts/andesites to significantly lighter values (δ^{49}Ti between -0.15 and $+0.08‰$), which is in agreement with a Rayleigh distillation model. The δ^{49}Ti correlates negatively with the abundance of Fe—Ti oxides, suggesting that in samples which have δ^{49}Ti signatures similar to those of arc-basalts, most of the Ti is hosted in pyroxene and amphibole. This indicates that the degree to which Ti isotopes are fractionated in a melt is controlled by the fraction of Ti incorporated into silicate phases versus that incorporated into Fe—Ti oxides.

In contrast, the corresponding Mo isotopic compositions of the upper crustal magmatic cumulates and mafic enclaves are more dispersed (δ^{98}Mo$_{NIST}$ = $-0.02 \pm 0.22‰$, 2 s.d.) and similar to average arc-basalts. However, Mo concentrations throughout several cumulate and mafic enclave bulk rocks measured are too enriched to be explained by pure fractional crystallization as they do not match modelled melt-cumulate fractionation trends. We distinguish between purely magmatic and predominantly fluid mediated processes leading to Mo enrichment in cumulates, and show that both can play an important role in the generation of high Mo cumulates.

1. Introduction

Modern arc-derived continental crust is mainly produced by fractional crystallization processes in the (lower) crust and upper mantle (Müntener and Ulmer, 2018). Mechanisms such as crystallization-differentiation, subduction erosion, delamination, or relamination that are responsible for the formation and modification of modern crust with an on average andesitic composition (e.g., Taylor and White, 1965; Rudnick, 1995; Jagoutz and Kelemen, 2015) are actively debated (Hacker et al., 2015). Early stages of magma differentiation in crustal reservoirs are witnessed by cumulate assemblages that evolve as counterparts of the liquid line of descent. These (deep) crustal snapshots of evolving magmatic systems provide insights into mass transfer processes during crustal growth.

For many non-traditional stable isotope systems, fractionation associated with igneous processes has been documented, indicating their potential to (i) advance our understanding of magmatic differentiation, (ii) reconstruct past geodynamic regimes, and (iii) perform mass balance calculations for the amount of extracted continental crust (e.g., Schuessler et al., 2009; Young et al., 2015; Millet et al., 2016; Aarons et al., 2020; Hoare et al., 2020). Molybdenum isotopes have been shown to record crustal extraction from the mantle (McCoy-West et al., 2019) and both, Ti and Mo isotopes fractionate during magma differentiation (Voegelin et al., 2014; Millet et al., 2016; Greber et al., 2017a, 2017b; Wille et al., 2018; Aarons et al., 2020; Hoare et al., 2020). Furthermore, Mo isotopes are also sensitive to high-temperature fluid processes within the crust (e.g., Greber et al., 2014; Shafiei et al., 2015; Kaufmann et al., 2021; Neely et al., 2018; Li et al., 2019). As Mo and Ti exhibit different

geochemical behaviour during magma evolution, they are promising candidates to trace different processes within the same sample record.

Molybdenum has been classified as a siderophile element (e.g. Goldschmidt, 1930) that is also moderately chalcophile (Lodders and Palme, 1991). With $D_{Mo}^{peridotite/melt} \sim 0.008$ during (arc) basalt genesis (Leitzke et al., 2017), Mo is highly incompatible affected by redox transitions in silicate systems (e.g. Righter et al., 2016). Light rare earth elements show similar compatibility while being partitioned between silicate and melt depending on their ionic radii (e.g. Newsom and Palme, 1984). Major known Mo carrier phases in crustal igneous rocks are titanite, magnetite, ilmenite, rutile, and volcanic glass (μg/g-level). Minor Mo hosting silicates such as biotite, amphibole, pyroxene, and garnet with lower concentrations (sub-μg/g-level) may still contribute significantly to the overall Mo mass balance, however, due to their higher modal proportions (Voegelin et al., 2014; Greaney et al., 2018). Molybdenum isotope variations in magmatic environments have been ascribed to processes such as magma differentiation due to mineral fractionation (e.g., Voegelin et al., 2014; Wille et al., 2018) and also subduction related slab-fluid migration into the fore-arc and mantle wedge (e.g., König et al., 2016; Chen et al., 2019; Ahmad et al., 2021). The enrichment of arc-basalts in heavy isotopes compared to the mantle is generally explained by the addition of heavy slab-derived components to the magmatic system, such as a fluid phase or sediments (Freymuth et al., 2015; König et al., 2016; Gaschnig et al., 2017; Chen et al., 2019; Ahmad et al., 2021). These isotopic signatures can subsequently be affected by late-stage magmatic-hydrothermal processes, e.g., in evolved (upper crustal) plutonic rocks where Mo enriched fluids exsolve from the solidifying magma (Kaufmann et al., 2021). Therefore, the $\delta^{98}Mo$ of arc lavas is variable but heavier on average ($+0.07 \pm 0.68‰$; Villalobos-Orchard et al., 2020) than the mantle ($-0.22 \pm 0.03‰$, Greber et al., 2015; Bezard et al., 2016; McCoy-West et al., 2019; Hin et al., 2022) and lighter than felsic volcanics (>63 wt% SiO_2; $+0.20 \pm 0.15‰$, Voegelin et al., 2014; Gaschnig et al., 2017; Wille et al., 2018) and granitoids (>63 wt% SiO_2; $+0.13 \pm 0.79$ ‰, Greber et al., 2011; Neubert et al., 2011; Voegelin et al., 2012; Yang et al., 2017; Kaufmann et al., 2021). The processes leading to a heavier Mo isotopic composition of evolved rocks compared to arc-basalts has remained a matter of debate (Fan et al., 2021; Chen et al., 2022; Ma et al., 2022). Importantly, information on calc-alkaline cumulates derived from a continental crustal setting that could represent the corresponding light reservoir balancing the heavy felsic lithologies as reported for layered intrusions of dry tholeiitic systems (Nebel-Jacobsen et al., 2021) is unavailable to date, despite the fact that cumulates represent a major constituent in modern arc crust.

In contrast to Mo, titanium is a refractory and (aqueous) fluid-immobile lithophile element (e.g., Audétat and Keppler, 2005; Rapp et al., 2010; Tropper and Manning, 2005) that behaves moderately incompatible during mantle melting $D_{Ti}^{peridotite/melt} < 1$ and has been used intensively as a petrogenetic tracer of magmatic rocks on Earth and other planetary bodies (e.g., Shervais, 1982; Pearce and Norry, 1979; Klemme et al., 2006). Numerous studies on natural magmatic rock suites coherent with fractionation experiments reveal that TiO_2 concentrations in melts (once saturated in TiO_2) correlate negatively with increasing SiO_2. This highly compatible behaviour ($D_{Ti}^{mineral/melt} > 1$) at low NBO/T (non-bridging oxygen per tetrahedra) ratios in calc-alkaline and tholeiitic melts (e.g. Farges and Brown Jr, 1997) is controlled by diverse factors including initial TiO_2 content (e.g. Mysen et al., 1980) of the melt, H_2O content and oxygen fugacity (fO_2) (e.g., Grove and Baker, 1984; Grove and Kinzler, 1986; Villiger et al., 2007; Nandedkar et al., 2014). The onset of Fe—Ti oxide crystallization and removal into mafic cumulates thereby strongly affects the TiO_2 budget of an evolving melt. Mass-dependent stable Ti isotope variations in igneous systems on Earth are therefore largely driven by magmatic processes (e.g. Millet and Dauphas, 2014; Millet et al., 2016; Greber et al., 2017a; Williams et al., 2021). Arc-basalts are isotopically lighter ($\delta^{49}Ti_{arc-basalt}$: $+0.018 \pm 0.045‰$; data from Millet and Dauphas, 2014; Millet et al., 2016; Greber

et al., 2017a; Hoare et al., 2020) than intermediate to highly evolved felsic rocks ($\delta^{49}Ti \sim 0.3$ to 2.4 ‰ at $SiO_2 \geq 65$ wt% SiO_2, arc and intraplate settings, respectively). Rhyolites from arc systems generally reach $\delta^{49}Ti$ values of up to 0.7‰, while samples from intraplate systems exhibit values as high as 2.4‰ (e.g., Deng et al., 2019; Aarons et al., 2020; Hoare et al., 2020; Zhao et al., 2020; Greber et al., 2021). The reason for the difference in the Ti isotopic composition between these magmatic series is debated, but likely primarily linked to the Fe and Ti contents of parental melts and the oxide mode (i.e. mainly ilmenite and/or magnetite) that fractionates (Aarons et al., 2020, 2021; Hoare et al., 2020, 2022).

Data from mineral separates of natural rocks (i.e. clino- and orthopyroxene, Fe—Ti oxides, olivine, plagioclase, biotite and quartz; Mandl, 2019; Nie et al., 2021; Greber et al., 2021; Rzehak et al., 2021; Anguelova et al., 2022) and in situ derived data obtained by micro-milling (Hoare et al., 2022) show that Fe—Ti oxides are isotopically light. Neso- and tectosilicates like olivine, quartz, and plagioclase are isotopically heavy, and amphibole and biotite exhibit intermediate $\delta^{49}Ti$ signatures (Mandl, 2019; Greber et al., 2021; Nie et al., 2021; Rzehak et al., 2021). These measurement data are in agreement with inter-mineral and mineral-melt experiments ranging from reduced lunar to more oxidized terrestrial conditions, (see Rzehak et al., 2021, 2022; Hoare et al., 2022) and ab-initio calculations (Leitzke et al., 2018; Wang et al., 2020; Aarons et al., 2021) at magmatic conditions and highlights the importance of Fe—Ti oxides as the driver of the observed Ti isotope fractionation during magmatic differentiation.

Both Mo and Ti isotope systems therefore require a light reservoir counterbalancing the heavy isotopic compositions of evolved continental rocks. Here we present a comprehensive Mo and the first Ti isotope bulk rock and mineral dataset for crustal mafic cumulates and enclaves from the Sanandaj Sirjan Zone (Siah-Kuh, Iran), the Alpine Orogen (Adamello, N-Italy), the Sierra Nevada Batholith (Onion valley, USA), and the Kos Plateau Tuff (Greece). Our data for arc-cumulate rocks allow to test the hypothesis whether cumulate materials represent the isotopically light reservoir counterbalancing the heavy evolved arc magmas, which has implications for the isotopic budgets of Ti and Mo of the continental crust.

2. Samples

2.1. Adamello batholith – Southern Alps (Italy)

The late Eocene to early Oligocene calc-alkaline Adamello batholith in the Southern Alps of Northern Italy comprises ultramafic to gabbroic rocks, associated with tonalites to granodiorites. We have analyzed three hornblendites (MAT2, MAT13 and MAT15, described in detail by Tiepolo et al., 2002, 2011) for their bulk rock and Mo and Ti isotopic compositions (Table 1). The investigated samples are mainly composed of pargasitic amphibole (75–80 vol%), olivine (15–17%), clinopyroxene (5–8%), and accessory oxides. Sample MAT-2 contains interstitial carbonate to amphibole grains (Tiepolo et al., 2011). These hornblendites are interpreted as the result of picritic basalt fractionation at pressures between 8 and 10 kbar prior to their shallow emplacement at 1–2 kbar based on geothermo−/barometry (Ulmer et al., 1983; Blundy and Sparks, 1992; Nimis and Ulmer, 1998).

2.2. Siah-Kuh intrusion – Sanandaj Sirjan zone (SSZ, Iran)

The Sanandaj Sirjan zone represents an Andean type continental margin of Mesozoic age hosting calc-alkaline gabbroic (Table 1) to granitic rocks that intruded Paleozoic to lower Mesozoic lithologies (Arvin et al., 2007). The oldest known intrusion is the Upper Triassic Siah-Kuh complex situated in the South East of the SSZ. It is characterized by numerous mafic enclaves within the granitoids that comprise olivine-hornblende pyroxenites (SKH11B, SKH11H) and olivine hornblendites (SKH11C). Associated mafic complexes in contact with the

Table 1
List of bulk rocks and mineral separates analyzed for Ti and Mo isotope compositions.

Sample	Rock type/mineral	Locality	TiO$_2$[wt %]	δ^{49}Ti[a][‰]	2 s.d.	n	Mo [μg/g][a,][b]	δ^{98}Mo[a][‰]	2 s.d.	n
Cumulates										
CA6	Olivine hornblendite	Onion Valley, Sierra Nevada batholith (California, USA)	1.36	−0.146	0.032	2	0.353	0.169	0.030	4
CA4C	Olivine hornblendite	Onion Valley, Sierra Nevada batholith (California, USA)	1.35	−0.150	0.032	3	0.579	0.076	0.030	3
CA3/6	Olivine hornblendite	Onion Valley, Sierra Nevada batholith (California, USA)	1.07	−0.092	0.032	2	0.707	0.153	0.030	3
CA9/2	Olivine hornblendite	Onion Valley, Sierra Nevada batholith (California, USA)	1.02	−0.092	0.032	3	0.417	−0.098	0.030	3
MAT2	Olivine hornblendite	Mt. Mattoni, Adamello batholith, Southern Alps (Italy)	0.61	0.001	0.032	2	0.470	−0.219	0.030	2
MAT15	Olivine hornblendite	Mt. Mattoni, Adamello batholith, Southern Alps (Italy)	0.59	0.014	0.032	2	0.680	−0.063	0.030	2
MAT13	Olivine hornblendite	Mt. Mattoni, Adamello batholith, Southern Alps (Italy)	0.60				0.690	0.007	0.030	1
SKH11B	ol-hbl pyroxenite	Siah-Kuh intrusion, Sanandaj Sirjan zone (Iran)	0.32	0.019	0.032	2	0.730	−0.145	0.030	2
SKH11C	ol-hornblendite	Siah-Kuh intrusion, Sanandaj Sirjan zone (Iran)	0.44	0.040	0.032	2	0.960	−0.115	0.030	2
SKH11H	ol-hbl pyroxenite	Siah-Kuh intrusion, Sanandaj Sirjan zone (Iran)	0.26	−0.006	0.032	1	1.060	−0.001	0.030	4
SKH12C	ol-gabbronorite	Siah-Kuh intrusion, Sanandaj Sirjan zone (Iran)	0.37	−0.002	0.032	1	1.418	−0.004	0.030	4
SKH12B	ol-gabbronorite	Siah-Kuh intrusion, Sanandaj Sirjan zone (Iran)	0.34	0.024	0.032	1	0.700	−0.040	0.030	3
KS08-83	cpx-hbl-mgt cumulate	Kos Plateau Tuff, Aegean arc (Greece)	2.37	−0.065	0.032	1				1
KS14-18	cpx-hbl-mgt cumulate	Kos Plateau Tuff, Aegean arc (Greece)	2.29	−0.068	0.032	3	0.320	−0.018	0.030	3
Mineral separates										
KS14-18	Clinopyroxene	Kos Plateau Tuff, Aegean arc (Greece)	1.77	0.091	0.032	6				
KS14-18	Amphibole	Kos Plateau Tuff, Aegean arc (Greece)	4.46	0.008	0.032	6				
KS14-18	Ulvospinel	Kos Plateau Tuff, Aegean arc (Greece)	14.40	−0.296	0.032	6				
Geostandards										
AGV-1	Andesite	Guano Valley (Oregon, USA)		0.124		1				
AGV-2	Andesite	Guano Valley (Oregon, USA)		0.096	0.034	4		−0.183	0.028	8
BCR2	Basalt	Columbia River (Oregon, USA)		0.028	0.018	2		0.060		1
BIR-1a	Olivine tholeiite	Reykjavik (Iceland)		−0.053	0.027	5				
G-2	Granodiorite	Westerly (Rhode Island, USA)		0.447	0.034	3				
RGM-1	Rhyolite	glass mountain (California, USA)		0.556	0.043	3				
W2a	Diabase	Centre Ville (Virginia, USA)						−0.079	0.037	3

Uncertainty on the external reproducibility of δ^{49}Ti data is estimated at ±0.032 ‰ and for δ^{98}Mo ± 0.030 ‰ based on the combined 2 s.d. of all measured geostandards, weighted for the number of repeated analyses.
[a] Average values of n-repeated analyses.
[b] Mo concentrations obtained by^{97}Mo—^{100}Mo double spike deconvolution.

granitoids of Siah-Kuh studied here consist of olivine gabbronorites (SKH12B, SKH12C). Exact conditions of emplacement are uncertain but field evidence suggests that mafic units and granitoids of Siah-Kuh are coeval.

2.3. Onion Valley – Sierra Nevada Batholith (USA)

The Onion Valley mafic composite intrusive complex formed over several magmatic episodes that built up the Mesozoic Sierra Nevada batholith (Sisson et al., 1996). Olivine hornblendites represent the most primitive crystallization products of the least evolved magmas of the Mesozoic Sierra Nevada batholith. The analyzed samples are from layered cumulate bodies that belong to the intrusive episode two as described in detail by Sisson et al. (1996). Samples CA4C and CA6 are from the same outcrop and are representative of the olivine hornblendites within sheeted sills. Samples CA3/6 and CA9/2 are equivalent of the former but representative of different horizons and were sampled in the talus. All olivine hornblendites (prefix CA; Table 1) show similar mineral modal compositions and are represented by a mass balanced mineral assemblage with ca. 40% olivine, 45% hornblende, 10% calcic plagioclase, 5% titanomagnetite, and a total of ca. 5% intercumulus phases such as biotite, orthopyroxene, intermediate plagioclase, and apatite possibly representing small amounts of former trapped liquid (see Sisson et al., 1996). Petrographic observations suggest that CA3/6

and CA6 are the most pristine samples followed first by CA4C that shows limited secondary/post-magmatic features of chloritization, and then CA9/2 that shows similar features and even contains some interstitial carbonates. The olivine hornblendites were sourced by high melt water concentrations (4–6 wt%) prior to their emplacement within the upper crust at pressures of ca. 2 kbar (Sisson et al., 1996).

2.4. Kos Plateau Tuff – Aegean arc (Greece)

The subduction related medium to high-K calc-alkaline series of the Kos Plateau Tuff hosts magnetite-clinopyroxene-plagioclase-hornblendites (KS14–18 and KS08–83, Table 1) described in detail by Gfeller (2016). They are interpreted as hydrous crustal derived cumulates that crystallized within a magma chamber affected by early amphibole crystallization as the result of fractional crystallization from basaltic andesite compositions (Hess, 2013; Gfeller, 2016). Trace element (mainly REE) matching compositions of amphibole cumulates and the co-genetic suite described by Voegelin et al. (2014) and Greber et al. (2021) make these cumulates witness of melt-cumulate segregation in differentiating magma chambers. Cumulates from the nearby Nisyros volcanic centre (10 km south of Kos) suggest cumulate formation depth at deeper crustal levels prior to emplacement in a shallow crustal magma chamber (Klaver et al., 2017, their type 3 cumulate). This is in general agreement with experimentally derived amphibole

compositions of Nandedkar et al. (2014). KS14–18 and KS08–83 are mainly composed of coarse-grained phenocrysts containing up to ca. 35% amphibole, ca. 30% clinopyroxene, ca. 10% plagioclase. Former interstitial melt (ca. 20%) is fully crystallized to amphibole, plagioclase and opaque minerals. Mineral separates of Ti-rich hornblende (c. 3.5–4.8 wt%), Ti-rich clinopyroxene (c. 1.7–2.5 wt%) and ulvospinel from KS14–18 were analyzed for their Ti isotopic values (Table 1).

3. Analytical methods

3.1. Bulk-rock major and trace element analysis

Dry splits of sample rock powders (<100 μm) used for isotope analysis were further processed to perform major and trace element measurements with LA-ICP-MS on "Nanoparticulate Pressed Powder Pellets"following the protocol of Peters and Pettke (2017) at the University of Bern (Supplementary Table A1).

3.2. Molybdenum isotope measurements

Rock samples between 0.5 and 2 kg were jacketed in aramid fabric prior to crushing to limit contact with metal. Crushed pieces were ground in a vibrating agate disc mill to <100 μm. Additionally, a lherzolite (PRE-1901) with a low Mo concentration from the Ivrea zone in northern Italy was treated identically (including milling) to validate contamination free sample processing. This lherzolite is well suited for this test as it is comparable to samples measured for Mo contents by Wang and Becker (2018) that yielded Mo concentrations below 30 ng/g. For Mo isotopic analysis 200–800 mg of rock powder was weighed into 25 mL Teflon beaker and mixed with a Mo double-spike solution, enriched in ^{97}Mo and ^{100}Mo. Samples were digested in an HNO_3 + HF mixture and subsequently dried down. Thereafter they have been digested in 6 M HCl to convert potential fluorides into chlorides. Dissolved samples were then dried down a second time and afterwards taken up in 4 M HCl to perform element matrix separation using Dowex AG1x8 (200–400mesh) anion exchange resin. Dried samples were taken up in 0.5 M HCl and further purified in a second step (Wille et al., 2013) using Dowex 50Wx8 (200–400mesh) cation exchange resin.

Stable Mo isotope ratios and concentrations were obtained by multiple-collector inductively coupled mass spectrometry on a NeptunePlus® MC-ICP-MS at the Isotope Geology laboratory at the Institute of Geological Sciences, University of Bern. Samples in 0.5 M HNO_3 were nebulised in a Cetac Aridus 2 desolvation unit with an uptake rate of 100μLmin^{-1} and transferred into the mass spectrometer. Five Mo isotopes (^{94}Mo, ^{95}Mo, ^{97}Mo, ^{98}Mo and ^{100}Mo) were measured at low resolution simultaneously in static mode on Faraday cups equipped with 10^{11} Ω resistors. Concurrently, ^{99}Ru and ^{101}Ru were monitored for potential interferences on ^{98}Mo and ^{100}Mo. No significant levels of Ru were identified, but ^{99}Ru correction was applied to account for potential minor interferences. Samples were bracketed by spiked NIST SRM 3134 solutions. Background correction was applied by measuring pure 0.5 M HNO_3 carrier solution intensities on-peak between sample analyses. Each sample and background measurement consisted of 40 cycles and a signal integration time of 4.192 s per cycle. Double-spike data reduction has been done offline by solving simultaneously three non-linear equations using the isotope ratios ^{97}Mo/^{95}Mo, ^{98}Mo/^{95}Mo and ^{100}Mo/^{95}Mo applying the exponential fractionation law (see Rudge et al., 2009; Greber and Van Zuilen, 2022). Sample-standard bracketing was performed using the NIST SRM 3134 standards measured before and after the unknowns. Total procedural blanks on Mo are below 4 ng, negligible compared to the total amount of >100 ng of Mo processed of each sample. The ultra-low concentraton Lherzolite (PRE-1901) from the Ivrea zone (N. Italy) yielded 26 ng/g of Mo in agreement with depleted mantle values of <30 ng/g reported from this area (Wang and Becker, 2018) and highlights low blank levels during sample processing.

All data are presented as the permil deviation of the ^{98}Mo/^{95}Mo ratio

relative to NIST SRM 3134 (Greber et al., 2012). To ensure data accuracy, geostandard powders W2a and AGV-2 were analyzed and treated identically throughout the course of this study. Analyses of geostandards AGV-2 and W2a with similar to lower Mo concentrations compared to our samples yielded $δ^{98}$Mo of $-0.183 \pm 0.028‰$ (2 s.d., $n = 8$) and $-0.079 \pm 0.037‰$ (2 s.d., $n = 3$), respectively and are identical within error to the average values reported by Burkhardt et al. (2014) and Willbold et al. (2016). Uncertainty on the external reproducibility of $δ^{98}$Mo data is estimated at $\pm0.030‰$, defined by the combined 2 s.d. of both measured geostandards, weighted for the number of repeated analyses (Table 1).

3.3. Titanium isotope measurements

Bulk rock isotopic compositions were obtained following the protocol of Greber et al. (2017b). Around 100 mg sample was fluxed with around 600 mg of ultrapure $LiBO_2$ at 1080 °C for 12–15 min in graphite crucibles. Pieces of homogenized $LiBO_2$ glass pellets containing ca. 6 μg Ti were weighed into Savillex beakers and mixed with ^{47}Ti—^{49}Ti double spike solution. Complete sample digestion was carried out in 10 mL of 3 M HNO_3 at 140–160 °C, dried down and redigested in 5 mL of 12 M HNO_3. Isolation of Ti from the matrix was carried out in a two-step ion exchange chromatography employing a 2 mL Eichrom TODGA column and subsequently Ti purification by 0.8 mL AG1-X8 Bio-Rad column chemistry (Zhang et al., 2011).

Ti isotopic compositions of the samples were determined using a NeptunePlus® MC-ICP-MS connected with an Aridus 3 desolvation unit at the University of Bern, measuring ^{46}Ti, ^{47}Ti, ^{48}Ti, ^{49}Ti and ^{50}Ti together with ^{44}Ca to correct for isobaric interferences from ^{46}Ca and ^{48}Ca on ^{46}Ti and ^{48}Ti, respectively. Measurements were performed in high resolution mode on peak shoulders below the polyatomic interference of ^{36}Ar^{14}N$^+$ on ^{50}Ti. Bulk rock samples were measured 2 to 3 times (80 cycles with 4.192 s integration time) except for mafic enclaves (SKH11H, SKH12B, SKH11C) which were measured only once. Ulvospinel, clinopyroxene, and amphibole mineral separates from cumulate sample KS14–18 from Kos were measured six times (100 cycles a 4.192 s). Double-spike data reduction has been done offline by solving simultaneously three non-linear equations using the isotope ratios ^{46}Ti/^{47}Ti, ^{48}Ti/^{47}Ti and ^{49}Ti/^{47}Ti, and applying the exponential fractionation law (see Rudge et al., 2009; Greber and van Zuilen, 2022). Sample-standard bracketing was performed using spiked Origins-Lab Ti standard (OL-Ti; Millet and Dauphas, 2014). Data accuracy was ensured by analyzing geostandards treated identically to the samples (Table 1). Measured $δ^{49}$Ti values yielded $+0.096 \pm 0.034$ for AGV-2, $+0.028 \pm 0.018$ for BCR-2, -0.053 ± 0.027 for BIR-1a, $+0.447 \pm 0.034$ for G-2 and $+0.556 \pm 0.043$ for RGM-1 and agree well with published data (Williams et al., 2021; Millet et al., 2016; Millet and Dauphas, 2014; Klaver et al., 2021; Greber et al., 2021). $δ^{49}$Ti values obtained for RGM-1 in this study are within uncertainty identical to reference material RGM-2 reported elsewhere (e.g., Hoare et al., 2020, 2022; Klaver et al., 2017; Millet et al., 2016). We like to note that the here obtained Ti isotopic composition of AGV-2 standard is identical to that from the data compilation by Williams et al. (2021). The $δ^{49}$Ti of standard AGV-1 however agrees only at the borders of the estimated uncertainties and might indicate that AGV-1 is slightly heterogeneous in respect to its Ti isotopic composition. Uncertainty on the external reproducibility of $δ^{49}$Ti data is estimated at $\pm0.032‰$ based on the combined 2 s.d. of all measured geostandards, weighted for the number of repeated analyses (Table 1).

3.4. Opaque mineral compositions by EPMA

The chemical composition of oxide minerals from six polished thin sections (CA4C, CA9/2, MAT2, SKH11B, SKH12C, KS14–18) were investigated at the University of Bern by electron probe micro-analysis (EPMA) using a JEOL-8200 Superprobe instrument equipped with 5 wavelength-dispersive spectrometers (WDS). Spot analyses were

acquired using a 1 μm electron beam diameter, 15 keV accelerating voltage and 20 nA specimen current. X-ray intensities were all obtained by WDS with 20 s counting time on peak positions and 10 s counting time on each background position (lower and upper). The following natural and synthetic standards were used for the CITZAF calibration: orthoclase (SiO_2), anorthite (CaO, Al_2O_3), magnetite (FeO), forsterite (MgO), rutile (TiO_2), Ni-metal (NiO), spinel (Cr_2O_3) and Pyrolusite (MnO).

3.5. MIA scan for determination of oxide and sulphide modes

Multiple image alignment (MIA) scans of thin sections were obtained using an OLYMPUS BX51 microscope equipped with a motorized stage and camera, remotely controlled by OLYMPUS Stream Motion (version 1.8 software). Image acquisition and treatment follows method described in Vieira Duarte et al. (2021). Images were acquired in reflected light, at maximum light intensity and using a 5× magnification lens. Acquisition parameters were adjusted at constant exposure time of 500 μs, ISO of 200, and using a stitching overlap of 20%. Final images were exported in TIFF format and compressed to 30% to enable image post-processing with ImageJ software (Schneider et al., 2012). Here, images were converted to 8-bit, and area selections corresponding to oxide and sulphide phases were created using grey-scale threshold intervals (ranging from 90 to 143, and from 143 to 234 for oxides and sulphides, respectively). For green spinel, images were acquired in transmitted light mode using very high light intensity for maximal brightness on spinel, and using a 5× magnification lens. Similar acquisition settings as for other oxides and sulphides have been used.
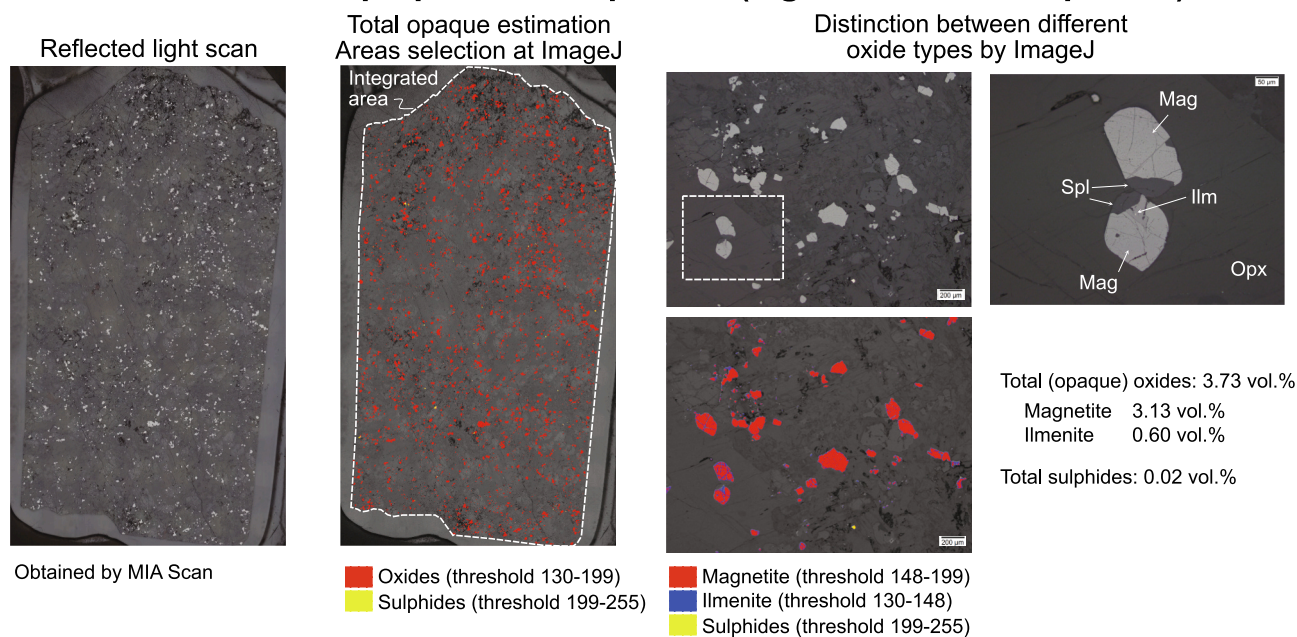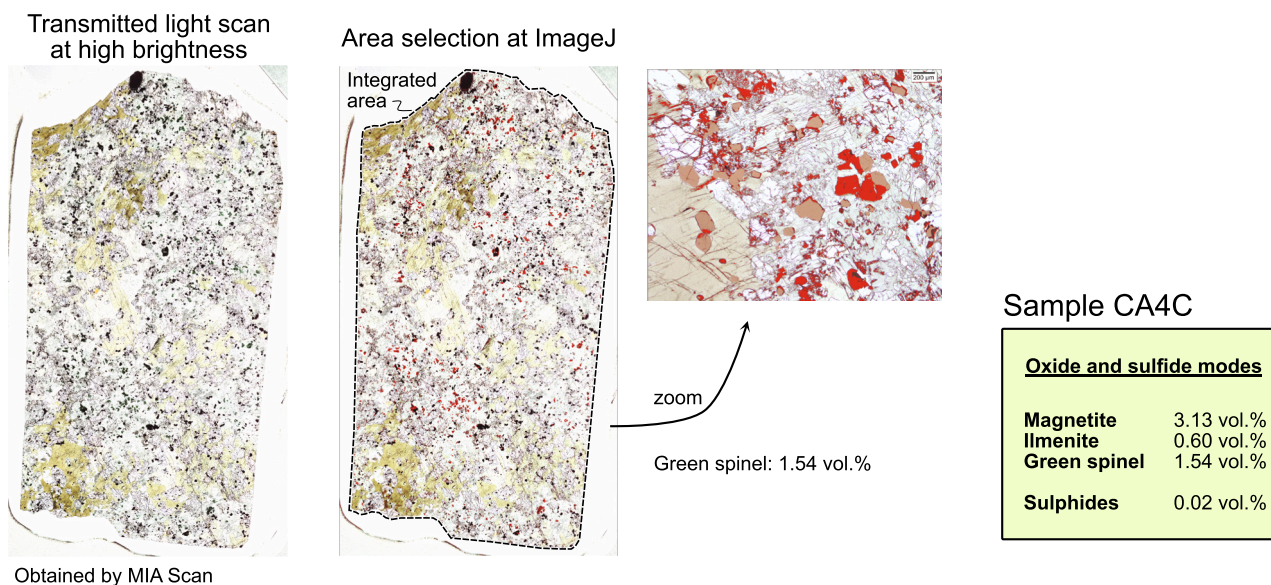

Fig. 1. Schematic workflow of opaque and transparent mineral phase estimation by reflected and transmitted light scans of thin sections. For detailed explanation of the method see main text.

However, post-processing in Image-J was done without converting the image to 8-bit, and by manually adjusting the colour threshold to the area of green colour corresponding to spinel. The selected threshold was manually verified to ensure that other green mineral phases (e.g. amphibole) were not selected.

The estimated image resolution of this method is ca. 5 μm, implying that sulphides and oxides with smaller size were not accounted for in calculated modes; hence, opaque mineral modes represent minimum estimates. We empirically propose an uncertainty of 10% for the modes of oxides and sulphides determined from (grey scale) image analysis. Schematic illustrations of the workflow, including an example can be found in Fig. 1.

4. Results

The following section summarizes our Mo and Ti isotopic data (Table 1) on mafic enclaves and cumulates and compares them with well characterized intermediate to evolved rocks from the Kos Plateau Tuff measured for their Mo and Ti isotopes, which were demonstrated to be dominated by fractional crystallization (Voegelin et al., 2014; Greber et al., 2021). All geochemical data including bulk rock major- and trace element compositions are summarized in Supplementary Tables A1, A2, A5, A6 and A9.

4.1. Titanium isotopes

All Ti isotopic data and bulk rock element compositions of measured samples and reference materials are provided in Table 1 and Supplementary Tables A2, A5, A6 and A9. Fig. 2 provides data from this study and the coherent Kos dataset of Greber et al. (2021). Cumulate samples and mafic enclaves broadly define a trend of increasing δ^{49}Ti with increasing SiO_2, extending the fractionation trend reported for Kos ranging from basalt to rhyolite (Greber et al., 2021) towards lighter Ti isotopic values. This trend is broadly similar for Ti isotopic compositions versus decreasing TiO_2, FeO_T, and V. Further arc related calc-alkaline volcanic rocks from Agung, Indonesia and Santorini, Greece (see Hoare et al., 2020; Millet et al., 2016), match the overall differentiation trend of δ^{49}Ti versus MgO and SiO_2 observed in samples from this study and Greber et al. (2021), while being shifted towards higher FeO_T (Agung) and higher TiO_2 (Santorini). Compositional offsets (e.g. MgO) of cumulates and in particular from mafic enclaves towards the fractionation pathway from Kos can be observed. Hornblendites from the Onion Valley intrusive complex with the highest FeO_T and lowest SiO_2 concentrations represent the lightest Ti isotopic values (δ^{49}Ti: −0.15 to −0.09‰), followed by cumulates from Kos with lower FeO_T but higher TiO_2 concentrations (δ^{49}Ti: −0.07‰), hornblendites from Adamello (δ^{49}Ti: +0.001 to +0.014‰) and mafic enclaves from Siah-Kuh represent the heaviest values (δ^{49}Ti: −0.01 to +0.04‰). Mineral separates from cumulate KS14–18 from Kos measured in this study are shown in Fig. 6, highlighting isotopically light Fe—Ti oxide values (δ^{49}Ti$_{ulvospinel}$: −0.30‰), heavy clinopyroxene and intermediate amphibole values (δ^{49}Ti$_{clinopyroxene}$: +0.09‰; δ^{49}Ti$_{amphibole}$: +0.01‰) relative to the bulk rock data (δ^{49}Ti$_{bulkrock}$: −0.07‰).

4.2. Molybdenum concentrations and isotopes

Molybdenum contents in cumulates and mafic enclaves reported here are highly variable on an inter- and intra-sample scale (e.g. see data from Kos) and range between 0.32 and 1.65 μg/g (Table 1, Fig. 3). The Mo isotopic compositions of all samples spread over a range of around 0.4‰ (δ^{98}Mo from −0.219 to +0.169‰) and overlap in δ^{98}Mo with those of arc basalts (45–55 wt% SiO_2) that average at −0.13 ± 0.43‰ (compiled from Freymuth et al., 2015, 2016; König et al., 2016;

Gaschnig et al., 2017; Ahmad et al., 2021; Voegelin et al., 2014; Wille et al., 2018; Li et al., 2021; Yu et al., 2022; Villalobos-Orchard et al., 2020). The samples from Siah-Kuh broadly define a positive linear correlation in δ^{98}Mo with differentiation indices of increasing silica, and decreasing magnesium and iron. Compared to the depleted mantle (Mo: ≤ 30 ng/g, δ^{98}Mo: −0.22 ± 0.03‰; e.g., Wang and Becker, 2018; Greber et al., 2015; McCoy-West et al., 2019; Hin et al., 2022) our samples have higher Mo contents and are overall isotopically heavier. Compared to evolved samples from Kos, granites from Torres del Paine and the granitic continental crust (δ^{98}Mo of ca. +0.13 to +0.20‰; Greber et al., 2011; Neubert et al., 2011; Voegelin et al., 2012, 2014; Kaufmann et al., 2021; Yang et al., 2017), the cumulates have significantly lighter δ^{98}Mo values. Comparison between δ^{98}Mo and δ^{49}Ti data of cumulate lithologies reveals no correlation (Fig. 3).

4.3. Opaque mineralogy in cumulates

The mineralogy of the Fe—Ti and Fe-Cr-Al oxides in the different samples is summarized in ternary classification diagrams (Fig. 4) and the corresponding data are provided in Supplementary Tables A3 and A4.

Magnetite is the main oxide phase in the three samples from the Onion Valley, Nevada (CA4C, CA6 and CA9/2) and makes up between 3.1 and 3.6 vol% of the rock. The magnetite grains are associated with c. 50 μm sized ilmenite (0.6 to 0.9 vol%), sharing straight boundaries in between two magnetite grains. All samples from the Onion Valley contain green, Al-rich spinel in variable modes, ranging from 0.3 to 2.4 vol%. In samples CA4C and CA6 they are observed together with magnetite, suggesting that they were formed by exsolution during cooling. Sulphides are minor (<0.05 vol%) and consist mainly of pyrrhotite with late chalcopyrite. The volumetrically quantified total oxide contents for samples from California (4.6 and 6.8 vol%) agree well with mass balanced opaque quantifications of 5 wt% reported from Sisson et al., (1996).

The three samples from Siah-Kuh, Iran (*SKH11B, SKH11C, SKH12B*) contain less oxides than those from the Onion Valley. Sample SKH12C contains 0.37 vol% magnetite. Sample SKH11B contains 0.3% magnetite, 0.35% Al-spinel and 0.14% Cr-spinel, and 0.12% ilmenite, summing up to a total oxide content of around 0.91%. In this sample, the dark-brown-coloured Cr-spinel cores are rimmed by Cr-magnetite mantles. All samples from Siah-Kuh contain more sulphides than found in the other localities, ranging from 0.16 to 0.30 vol%. In sample SKH11B, which contains the highest amount of sulphides, euhedral pyrrhotite and pentlandite grains can reach 1 mm in size, with chalcopyrite replacing pentlandite/pyrite at a later stage.

The sample analyzed from Adamello, Italy (MAT2) contains around 0.92 vol% magnetite that forms graphic intergrowth textures with silicates. Only few (0.05 vol%) sulphides are found, identified as pentlandite and locally retrograde chalcopyrite.

Sample KS14–18 from Kos contains oxides that are compositionally between ulvospinel and magnetite and that form either ca. 500 μm size anhedral inclusions in silicate minerals or very small 10–25 μm size graphic textures in the matrix. For this sample, it is difficult to precisely estimate the total amount of oxides due to the coarse-grained nature of the silicate phases on a thin section scale. In this sample we also analyzed the Ti concentrations and isotopic compositions of major Ti hosts (see Table 1 and Tables A5 and A6; clinopyroxene, hornblende and ulvospinel in KS14–18), allowing us to estimate the abundance of oxides by mass balance calculations. The quantification of the abundance of the oxide phases by MIA Scan range between 1.1 vol% for image analysis and 2.7 vol% for mass balanced abundance, respectively. We therefore regard this latter value as more accurate than the lower MIA scan estimates, possibly resulting from the fact that interstitial oxide phases smaller than 5 μm are not recognised by MIA scan. Sulphides are rare
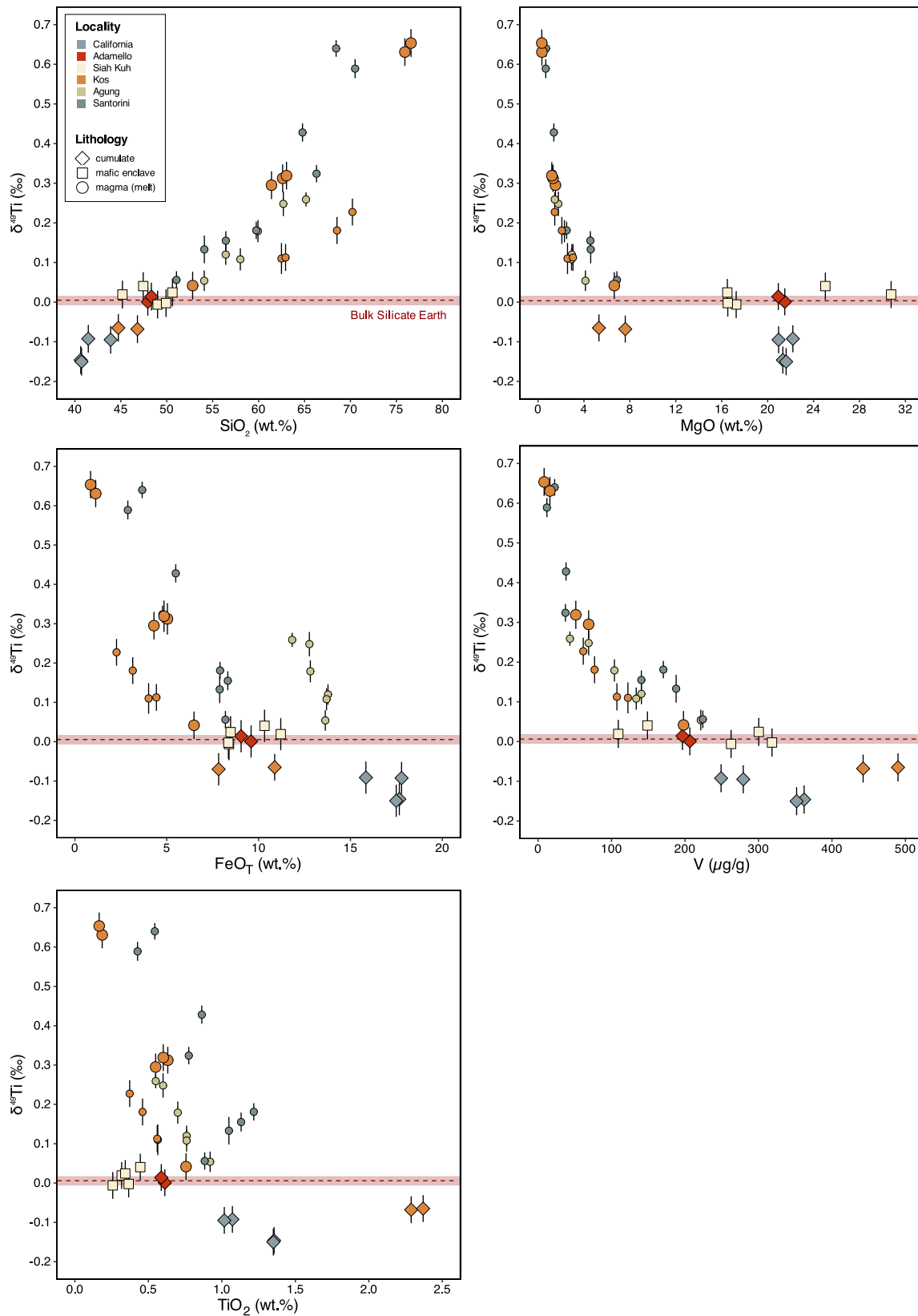
Fig. 2. Major and trace element versus Ti isotope values of cumulates and mafic enclaves compared to data from evolved rocks from Kos (Greber et al., 2021), Agung (Hoare et al., 2020) and Santorini (Millet et al., 2016). Small orange circles from Kos indicate samples potentially affected by magma mixing (Greber et al., 2021), while big orange circles represent melts dominated by fractional crystallization. Red dashed line marks the Bulk Silicate Earth value of $\delta^{49}Ti_{BSE} = +0.005 \pm 0.012‰$ as defined by Millet et al. (2016). Uncertainties for $\delta^{49}Ti$ data from literature were taken as listed by the authors and can differ from the 2 s.d. reported for our analyses (i.e., 95% c.i. or 2 s.e.). (For interpretation of the references to colour in this figure legend, the reader is referred to the web version of this article.)
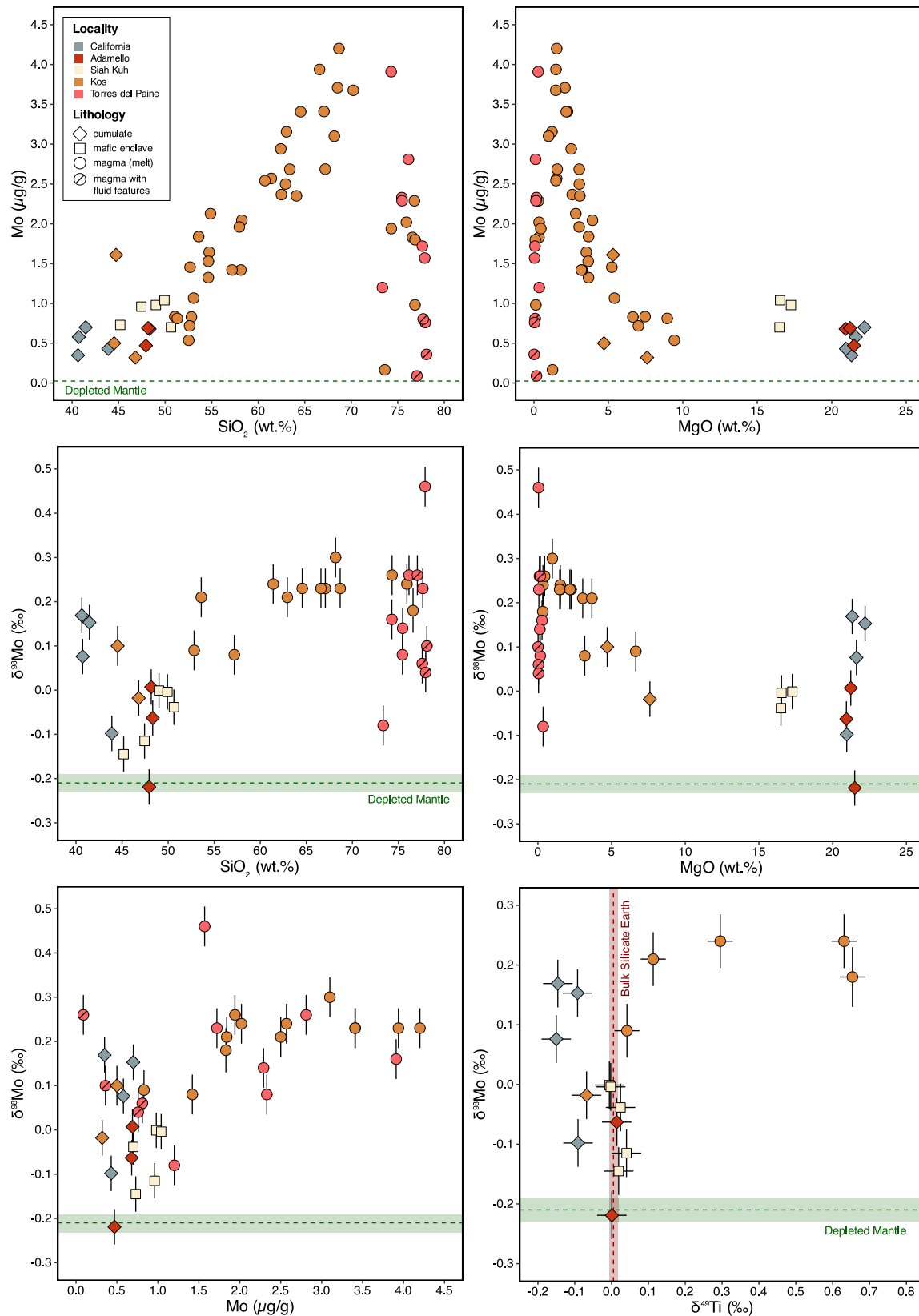
Fig. 3. Major element and isotope data of cumulates, mafic enclaves and melts compared with data from Kos (Greber et al., 2021; Voegelin et al., 2014) and Torres del Paine (Kaufmann et al., 2021) (see Supplementary Table A2, A5, A6 and A9). Dashed green lines indicate Mo concentration (<30 ng/g, Wang and Becker, 2018) and Mo isotopic composition of the depleted mantle ($-0.22 \pm 0.03‰$, e.g. Greber et al., 2015; McCoy-West et al., 2019; Hin et al., 2022). Red dashed line corresponds to the average $\delta^{49}Ti$ value of the Bulk Silicate Earth ($+0.005 \pm 0.012‰$; Millet et al., 2016). Uncertainties for isotope data from literature were taken as listed by the authors and can differ from the 2 s.d. reported here for our analyses (i.e., 95% c.i. or 2 s.e.). (For interpretation of the references to colour in this figure legend, the reader is referred to the web version of this article.)
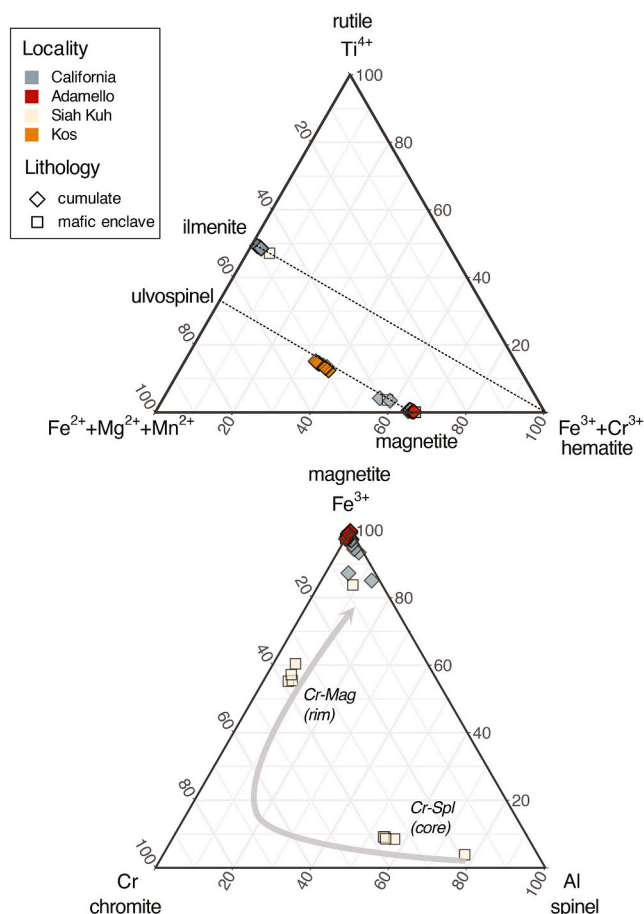
Fig. 4. Ternary classification diagrams of Fe—Ti oxides (upper ternary plot) and Fe-Cr-Al oxides (lower ternary plot) measured by EPMA. Upper diagram: Black dashed lines indicate solid solutions between magnetite-ulvospinel and hematite-ilmenite, respectively. Lower diagram: Grey arrow schematically marks the typical evolution of oxides upon cooling leading to coexisting Cr-spinel and Cr magnetite for samples from Siah-Kuh.

and make up <0.01 vol% of the rock.

5. Discussion

5.1. Controls on the titanium isotopic composition of cumulate rocks

Magmatic differentiation suites display an increase in δ^{49}Ti with progressive magma differentiation relative to indices such as SiO_2 or MgO (Fig. 2). Provided that observed trends in δ^{49}Ti versus SiO_2 are the product of dominant fractional crystallization, one can quantify the Ti isotope fractionation factor between melt and crystallizing minerals (Δ^{49}Ti$_{solid-melt}$). We follow a published approach that uses highly incompatible element concentrations of a rock series (e.g., K_2O, Rb, Th) for which a partition coefficient of 0 can be assumed, allowing us to approximate the fraction of Ti residing in a melt (f_{Ti}) (see Greber et al., 2021; Teng et al., 2008; Hoare et al., 2020) through:

$$f_{Ti} = \frac{[Ti]/C}{[Ti]_0/C_0} \qquad (1)$$

Here, C and C_0 are the concentrations of a highly incompatible element in the sample and the most primitive melt, [Ti] and [Ti]$_0$ are the Ti concentrations of the sample and the most primitive melt. Knowing f_{Ti} and the Ti isotopic composition of a rock enables to estimate Δ^{49}Ti$_{solid-melt}$ using a Rayleigh distillation model for fractional crystallization:

$$\delta^{49}Ti \simeq \delta^{49}Ti_0 + \Delta^{49}Ti_{solid-melt} ln f_{Ti} \qquad (2)$$

with δ^{49}Ti being the isotopic composition of the sample and δ^{49}Ti$_0$ being the initial isotopic composition of the system. Applying this method to published δ^{49}Ti values of arc-related rocks for which fractional crystallization has been suggested to be the dominant process of magma differentiation yields a Δ^{49}Ti$_{solid-melt}$ of −0.18‰ (see Fig. 6; Agung and Santorini systems from Hoare et al., 2020; Kos magmatic suite from Greber et al., 2021) when assuming an initial δ^{49}Ti$_0$ of +0.024 ± 0.043‰ (average calc-alkaline arc basalt derived from literature compilation, see Table A9). The estimated Ti isotope fraction between crystalizing solids and melt of −0.18‰ for calc-alkaline systems agrees also with that calculated for two synthetic mixtures of typical cumulate mineral assemblages closely matching the presented datasets for Kos and California at around 1000 °C, resulting in a Δ^{49}Ti$_{solid-melt}$ of between −0.16‰ and − 0.08‰ (Supplementary Table A10). The two modelled mass-balanced analogue compositions employ mineral-melt partition coefficients from the literature except for amphibole where we assume a Δ^{49}Ti$_{amphibole-melt}$ of −0.05‰.

Assuming that evolved melt above around fTi = 0.1 (i.e. ~65 wt% SiO_2) no longer produces ortho- but rather meso- to adcumulates in the upper crust due to high melt viscosities at low porosities hindering mineral-melt segregation (e.g. Lee et al., 2015), the model predicts that instantaneous and bulk arc-cumulates have δ^{49}Ti values in the range from around −0.16 to around +0.05‰ (see Fig. 6). These calculations therefore agree well with our measured Ti isotope data on calc-alkaline arc-cumulates (see Figs. 1, 4, 5).

While the cumulates investigated here extend the linear correlation between δ^{49}Ti and SiO_2 concentrations of evolved rocks, no correlation is observed between the Ti isotopic compositions and the MgO and Ni contents of the cumulates (Fig. 2, Fig. A1). Both elements are highly compatible in early crystallizing minerals, implying that the earliest produced cumulates during fractional crystallization do not necessarily contain the lightest Ti isotopic composition. Effects of secondary processes on the rather conservative Ti inventory of magmatic rocks is likely small (e.g., Giere, 1990), as Ti remains immobile unless elevated pressures and chloride/fluoride-rich conditions are reached (e.g., Tropper and Manning, 2005; Audétat and Keppler, 2005; Rapp et al., 2010). For example, the δ^{49}Ti signature of eclogites, subduction derived serpentinites and arc-basalts do not indicate that subduction zone fluids exert a strong impact on Ti isotopes of arc-basalts (Millet et al., 2016). However, stronger Ti isotope variability has been documented for orogenic peridoties from the Horoman massif (Anguelova et al., 2022).

Cumulates witness single or multiple stages in fractionating magmatic systems, partially recorded by compositionally zoned minerals like clinopyroxene or amphibole (e.g. Klaver et al., 2017). This evolution can be accompanied by numerous processes such as assimilation of plutonic roots (e.g., Reubi and Blundy, 2008; Blundy and Sparks, 1992) due to magma mixing or mingling, mafic rejuvenation (including variations in source compositions, fO$_2$, and water content, e. g., Storck et al., 2020, 2021) and limited mechanical separation of melt and cumulate minerals leading to the retention of interstitial melt of variable compositions (e.g., Elkins-Tanton et al., 2011; Krättli and Schmidt, 2021). All of these processes would shift the δ^{49}Ti signature of a cumulate towards heavier values when compared to a single-stage cumulate formation early on in a fractionating magmatic system, thus likely contributing to some of the spread observed in our dataset. Indeed, we observe a within-sample correlation between δ^{49}Ti and highly incompatible element (e.g. Th or Ce) concentrations which could suggest that the variable Ti isotopic compositions of cumulate rocks are affected by variable fractions of (late) interstitial melt (Fig. A1b, c). However, no correlation is found between samples from different locations.

Amphibole and clinopyroxene in the Kos cumulate KS14–18, for which we obtained δ^{49}Ti data for mineral separates, are Ti-rich and
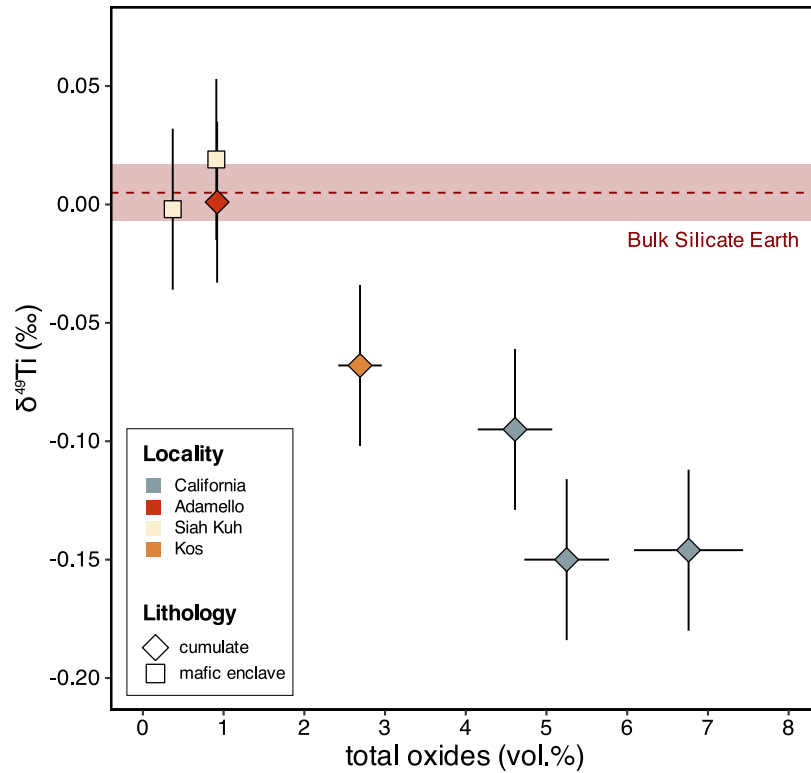
Fig. 5. Volumetrically quantified oxide versus bulk rock Ti isotope signature according to workflow presented in Fig. 1. Note that δ^{49}Ti values correlate negatively with increasing amount (vol%) of various oxide types.

zoned. From core to rim, TiO_2 concentrations in the amphibole and clinopyroxene increase from 3.8 to 4.8 wt% and from 0.8 to 1.8 wt%, respectively. These mineral zoning patterns and the peritectic growth of

amphibole at the expense of clinopyroxene (clinopyroxene + melt ➔ amphibole; amphibole replacing clinopyroxene observed in KS14–18), record a continuous evolution of this cumulate (e.g. in a mushy regime).
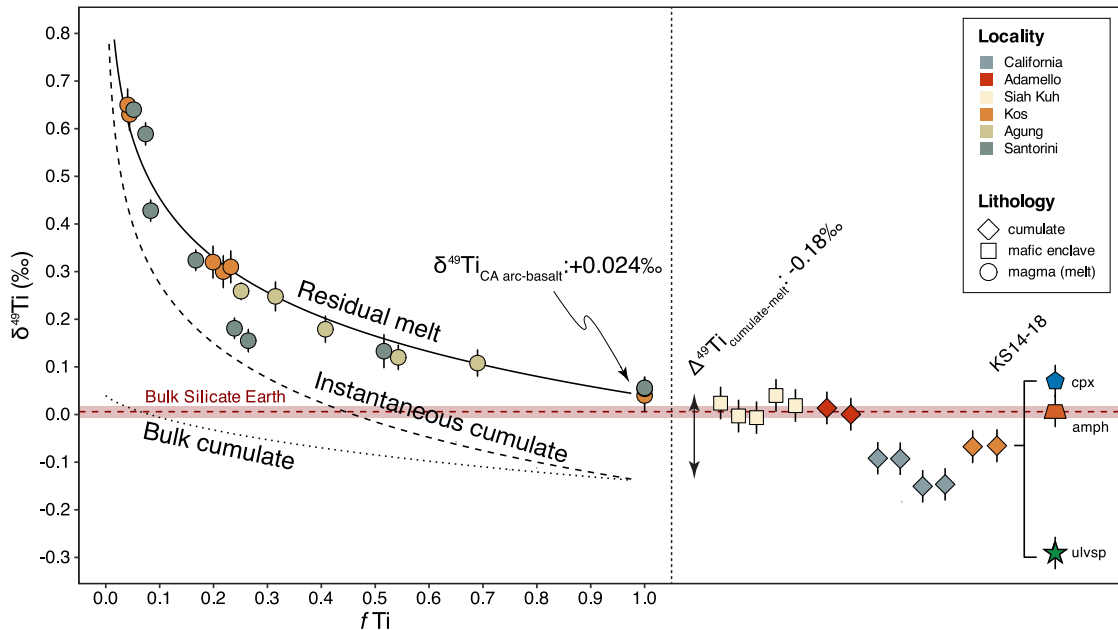

Fig. 6. Rayleigh distillation model for arc-related Ti isotope fractionation (left panel). Bulk rock stable-isotope fractionation factor calculated based on samples predominantly formed by fractional crystallization and by employing incompatible element concentrations (K_2O, Rb and Th) to approximate the fraction of Ti (fTi) that resides in the melt. Ti-isotopic and fTi data for Agung and Santorini were taken from Hoare et al. (2020) and for Kos recalculated from Greber et al. (2021). Input parameters applied to the model can be found in Supplementary Table A8. Cumulate rocks (right panel) measured in this study cover the expected range of δ^{49}Ti values (-0.14 to $+0.04$‰) from the model with Δ^{49}Ti$_{cumulate-melt}$ of -0.18‰. Clinopyroxene (cpx), amphibole (amph) and ulvospinel (ulvsp) represent major Ti carrier phases (Table 1) dominating the δ^{49}Ti signature of cumulate KS14–18.

Clinopyroxene and amphibole separates have a δ^{49}Ti of +0.09‰ and +0.01‰, respectively, and are thus heavier than the bulk rock value of −0.07‰. The isotopic composition of the amphibole mineral separate is identical to that of a basaltic melt and might be the result of amphibole crystallizing by the interaction between a trapped melt and clinopyroxene. The only mineral that contains significant amounts of TiO_2 and that is lighter than the bulk rock is ulvospinel (Figs. 4 and 6; TiO_2 ∼ 14.4 wt%; δ^{49}Ti = −0.30‰). The isotopic composition of the melt crystallizing these minerals was likely in-between the δ^{49}Ti of the pyroxene (heavier than melt; Wang et al., 2020; Rzehak et al., 2021) and the amphibole (lighter than melt; Mandl, 2019), leading to a δ^{49}Ti$_{ulvospinel-melt}$ of −0.35 ± 0.05‰ (with δ^{49}Ti$_{a-b}$ = δ^{49}Ti$_a$ - δ^{49}Ti$_b$). Using the calibration of Hoare et al. (2022) (see their Fig. 8A), this difference in the Ti isotopic composition between ulvospinel and melt suggests a crystallization temperature of ulvospinel between 1090 °C to 1300 °C. The lower end of the estimated temperature is a bit higher than the stability field of typical arc derived calc-alkaline amphibole (≤1010 °C, Nandedkar et al., 2014; ≤990 °C, Marxer et al., 2022), however, Ti isotope fractionation between mineral and melt as a function of temperature is not fully calibrated yet. The reasonable crystallization temperature estimate of ulvospinel based on its Ti isotopic composition therefore indicates that the minerals measured in sample KS14–18 record close to magmatic δ^{49}Ti values. The results from the mineral separates also suggest that at least for cumulate assemblages, which are fractioned from basaltic to andesitic melts, Fe—Ti oxides are the major Ti phases that have a significantly light Ti isotopic signature compared to the coexisting melt. We mention here that the Ti isotope fractionation between melt and amphibole is uncertain and needs further investigation.

The cumulate samples from Adamello and Siah-Kuh do not have a lighter δ^{49}Ti value than an average arc basalt. The samples from Adamello are hornblendites and thus have high amounts of amphibole compared to relatively low oxide abundances (Fig. 4; 0.92 vol% oxides in MAT2) and the oxides are dominantly magnetite (Table A4). The mafic enclaves from Siah-Kuh also have low oxide abundances dominated by magnetite (Fig. 5; 0.37 to 0.91 vol% oxides). We therefore recognise a good correlation between the δ^{49}Ti and the estimated vol% of oxides among our samples (Fig. 5) indicating that the latter exerts the most important control on the Ti isotopic composition of arc-cumulate rocks and therefore also on the isotopic value of the co-evolving melt.

5.2. Molybdenum isotopic composition of cumulates

Molybdenum is an incompatible element and thus becomes enriched in the melt during fractional crystallization. Volcanic rocks whose chemical signatures are dominated by fractional crystallization show Mo enrichment with progressing magma differentiation. In the example from Kos, Mo contents increase from ca. 0.5 to 4.5 µg/g Mo from basalt to rhyodacite and rhyolite, respectively (Fig. 3). This holds true to about 70 wt% SiO_2, above which Mo contents start to decrease again with increasing SiO_2. This has been interpreted to be due to Mo removed from the system by exsolving hydrothermal fluids (Kaufmann et al., 2021), supported by measured $D_{Mo(fluid/melt)}$ of ca. 10 at fluid exsolution from crystallizing granite (Audetat and Pettke, 2003). Arc lava suites such as rocks from Kos and Banda arc (Indonesia) also exhibit Mo isotope ratios evolving towards heavy values from basalt to rhyolite (e.g., Voegelin et al., 2014; Wille et al., 2018). Larger spread in δ^{98}Mo of highly evolved rocks (e.g. from Torres del Paine) was interpreted as isotope fractionation related to progressive late stage exsolution of a Mo bearing fluid-phase from a solidifying magma.

Given the fact that felsic upper crustal lithologies (δ^{98}Mo of c. +0.13 to +0.2‰; Greber et al., 2011; Neubert et al., 2011; Voegelin et al., 2012, 2014; Kaufmann et al., 2021; Yang et al., 2017) are on average heavier than arc-basalts (δ^{98}Mo of c. -0.13 ± 0.43‰; Freymuth et al., 2015, 2016; König et al., 2016; Gaschnig et al., 2017; Ahmad et al., 2021; Voegelin et al., 2014; Wille et al., 2018; Li et al., 2021; Yu et al., 2022; Villalobos-Orchard et al., 2020), one would expect the occurrence

of a light reservoir in the continental crust counterbalancing these heavy values. Our new δ^{98}Mo values for mafic enclaves and cumulates (Fig. 3) are, however, isotopically similar to common arc-basalts (Table 1, Fig. 3), but they are also much more enriched in Mo than expected when fractional crystallization was the main process controlling their Mo inventory. Experimentally derived elemental Mo partitioning between magnetite and a CaO–FeO–SiO_2 melt system at fO_2 of NNO to NNO + 1 results in $D^{mgt-melt}$ of 0.098 to 0.015 at 1150 °C (Sievwright et al., 2020). For silicate phases like pyroxene and olivine, Mo partition coefficients are equally low (e.g., Wijbrans et al., 2015; Leitzke et al., 2017). We have calculated a simplified Mo concentration Rayleigh distillation model for a basaltic melt evolving towards a rhyolitic composition (Fig. 7). The model calculations are based on initial Mo concentrations of a primitive basalt from Kos (0.55 µg/g Mo at 51 wt% SiO_2 and 9 wt% MgO) using melt-cumulate partition coefficients of 0.015 and 0.098 for Mo, and 0.86 as well as 1.9 for SiO_2 and MgO, respectively (Supplementary Table A7). The partition coefficients for SiO_2 and MgO have been chosen so that after around 80% crystallization of the system their concentrations in the melt are ca. 65 wt% and 2 wt%, respectively, in order to agree with experimental data for arc-melt evolution (Nandedkar et al., 2014). Calculated melts closely overlap with the rock suite from Kos until around 70 wt% SiO_2, after which Mo concentrations are impacted by fluid exsolution processes.

Importantly, most cumulates and mafic enclaves measured here are significantly more enriched in Mo (0.32 to 1.65 µg/g) compared to the results predicted from fractionation modelling, even when the higher cumulate-melt partition coefficient of 0.098 is used (resulting in 55 to 200 ng/g Mo in the cumulate). The resulting discrepancy between calculated and naturally occurring cumulates may have several reasons. Firstly, the modelled analogue with input parameters from Kos may deviate for all other cumulates analyzed in this study. However, even if the initial Mo concentration of the other magmatic systems were higher, the strong incompatibility of Mo would still predict cumulates with lower Mo concentrations than observed. Some magmatic sulphides can host Mo and their impact on the liquid line of descent might not be accurately predicted by our model. There is a weak correlation between the Mo concentration and the estimated vol% of sulphides, as well as with the Se concentration (used as proxy for sulphide abundance; see Jenner et al., 2010) in our cumulates (see supplementary Fig. A3). However, also samples with very low amounts of sulphides and Se show elevate Mo concentrations. We also rule out that the high Mo concentrations result from our sample processing procedures, as we obtained very low Mo concentrations for an identically treated peridotite sample (PRE19-01 yielding 26 ng/g Mo).

Molybdenum is well known to be preferentially transported in hydrothermal fluids (e.g., Audetat and Pettke, 2003; Zajacz et al., 2008; Tattitch and Blundy, 2017); hence, it can be hypothesized that cumulates may have been overprinted by percolating magmatic-hydrothermal fluids unmixed for example from deeper-seated mafic magma reservoirs. To test this hypothesis, we plot a fluid-mobile incompatible trace element (Mo) versus a fluid-immobile trace element (Th) and both normalized to a strongly compatible element (e.g. MgO) of a magmatic system dominated by fractional crystallization. The resulting melt-cumulate evolution curves of these ratios should positively correlate (linearly when plotted in log-scale), even when comparing samples from different locations (Fig. 8a), unless fluid-mediated enrichment or depletion processes affected a given rock. Fig. 8b illustrates the comparison of measurement data of all samples employed in this work compared to modelled compositions of melt and related instantaneously formed cumulates (in percent) with progressive fractionation. Model input parameters are based on data from Kos ($D_{Th}^{solid-melt}$ = 0.01, Th$_{initial}$ = 1.4 µg/g and $D_{Mo}^{solid-melt}$ = 0.015 at NNO + 1, Mo$_{initial}$ = 0.55 µg/g). While Ce/MgO vs. Th/MgO ratios of the melt and cumulates display a very good positive correlation demonstrating magmatic control for these elements, several cumulates deviate from the predicted purely magmatic Mo/MgO v Th/MgO evolution.
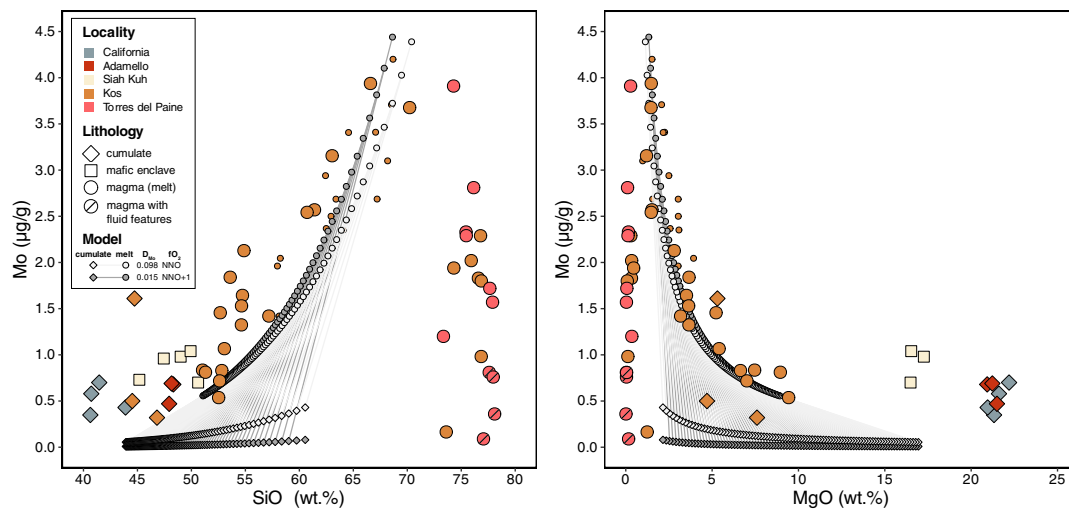
Fig. 7. Molybdenum contents [μg/g] of cumulates, mafic enclaves and melts versus SiO$_2$ and MgO (wt%). Mo concentration data for Kos (orange) are from Voegelin et al. (2014), Greber et al. (2021) and this study. Small orange points correspond to samples affected by magma mixing (see Greber et al., 2021). Upper crustal granites from Torres del Paine were taken from Kaufmann et al. (2021). Granites with obvious fluid features are highlighted as slashed circles. Modelled Rayleigh distillation curves for melt-oxide pairs of the Kos suite are shown as coloured lines between symbols corresponding to NNO (light grey, D^{Mo}: 0.098) and NNO + 1 (dark grey, D^{Mo}: 0.015) according to melt-magnetite partitioning experiments from Sievwright et al. (2020). Input parameters are similar to those introduced in Fig. 6 and can be found in Supplementary Table A7. Bulk Mo concentrations of naturally occurring upper crustal mafic lithologies are orders of magnitudes more enriched in Mo than estimates based on the Kos magmatic suite.
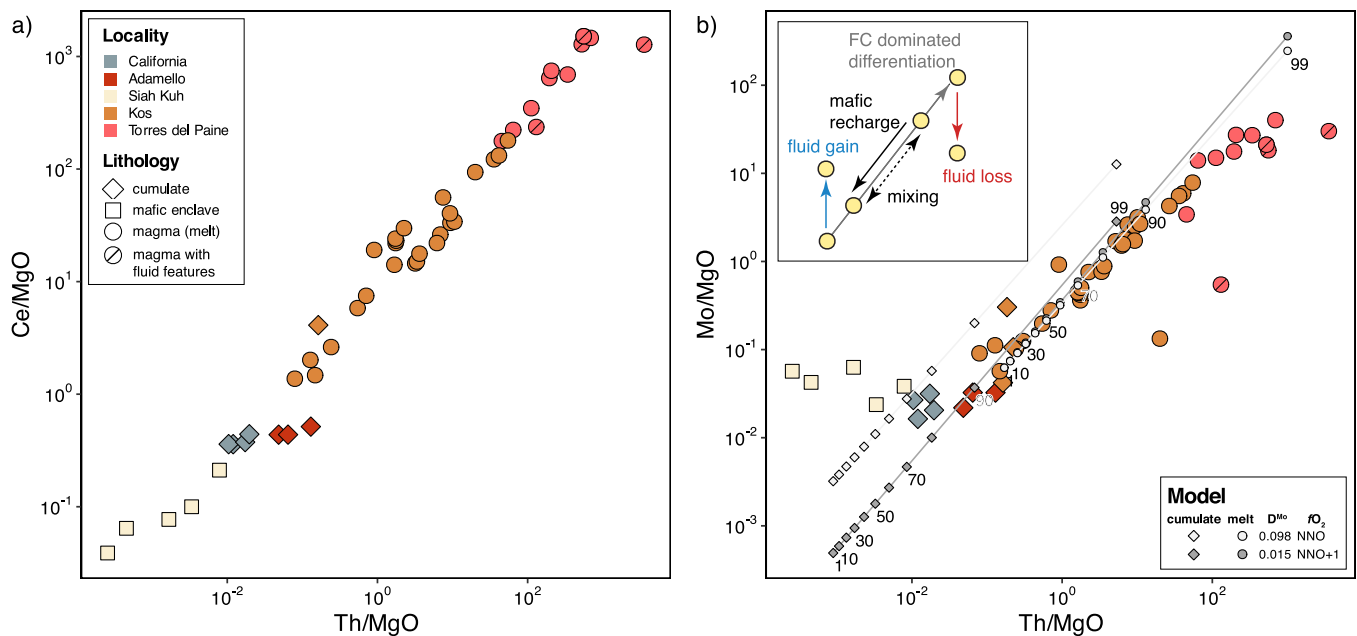

Fig. 8. MgO (wt%) normalized ratios of highly incompatible and fluid-immobile (Th and Ce) versus highly incompatible and fluid-mobile Mo (μg/g) for cumulates, mafic enclaves and arc derived volcanic and intrusive rocks from Kos (Voegelin et al., 2014; Greber et al., 2021) and granites from Torres del Paine (Kaufmann et al., 2021). Circles correspond to modelled melt compositions and diamonds represent related instantaneously formed cumulates (between 1 and 99%) with D$_{Th}$ $^{solid-melt}$ = 0.010, Th$_{initial}$ = 1.4 μg/g and D$_{Mo}^{solid-melt}$ = 0.015 (dark grey), D$_{Mo}^{solid-melt}$ = 0.098 (light grey), Mo$_{initial}$ = 0.55 μg/g. Inlet upper left schematically shows processes shifting samples away from the "ideal" fractional crystallization (FC) trend due to fluid-mediated Mo gain (samples above FC trend) or fluid-mediated Mo loss (samples below FC trend) as shown for granites at Torres del Paine with obvious fluid features (slashed circles) and without (Kaufmann et al., 2021). Note, that magma mixing would shift the data point along the magmatic fractionation line (FC) up or down (dashed black arrow), mafic rejuvenation of a magma reservoir by a source stable in initial Mo and Th composition would drag down the melt composition and lift infiltrated cumulate mush zones.

Towards the highly fractionated felsic side in Fig. 8, we observe that most granitic and rhyolitic rocks deviate towards lower Mo for a given Th concentration, and those from Torres del Paine displaying magmatic-hydrothermal fluid saturation features (Kaufmann et al., 2021) are displaced the strongest. This is in agreement with the implication that rocks displaying magmatic-hydrothermal fluid saturation features have

lost a fraction of their Mo budget into the exsolving magmatic hydro-thermal fluid that escaped the sampled rock volume. One granite from Kos (KS14–42, Supplementary Table A9) clearly plots below the frac-tionation trend observed for rocks from Kos in Fig. 8b. This sample has higher MgO concentrations than expected from its elevated SiO$_2$, Th and LREE signature, shifting its Th/MgO ratio to somewhat lower values. We

argue based on the elevated concentration of incompatible elements like Th together with the low Mo concentration of this granite (0.17 μg/g) that this sample experienced fluid loss, too.

Cumulates from Kos and Adamello hornblendites lie on the modelled melt-cumulate evolution curve, but would imply to be cumulates from an unrealistically late melt (after crystallization of ~90%, Fig. 7b). Cumulate data from California plot also above the trend given for the Mo partition coefficient at NNO + 1 (i.e. 0.015), but they would agree if in this system the melt-bulk cumulate partition coefficient of Mo was around 0.098 (Fig. 8; light grey curve with diamonds). But also here, the model would infer that the cumulates were formed very late. The combined high Mo and Th concentrations of these cumulates might therefore witness incomplete melt-cumulate segregation or infiltration of a cumulate mush by a fertile melt (i.e., mafic rejuvenation as reported from other provinces in the Southern Alps; Storck et al., 2020, 2021).

The effect on the concentration and isotopic composition of processes like retention of interstitial melt or mafic rejuvenation would be significantly more severe for an incompatible element like Mo than for Ti. However, the effect of variable fractions of intercumulus melt in the cumulate on the Mo concentration should affect other incompatible elements too, including, Th, La or Hf (Fig. A2). While all of the latter three elements correlate positively with each other, overall, they do not exhibit a positive correlation with Mo. If melt retention or rejuvenation were the processes responsible for the high Mo concentrations and variable isotopic compositions, then the contaminating material needed to have distinct and variable Mo/Th, Mo/Hf and Mo/La ratios, even for samples from the same location.

Cumulates from Siah-Kuh plot clearly above the magmatic fractionation line defined by the Mo/MgO vs Th/MgO ratios (Fig. 8), indicating that these rocks were affected by a high Mo, low Th media, rendering processes like mafic rejuvenation, or incomplete melt-cumulate segregation unlikely. Due to the high fluid mobility of Mo, we thus suggest that Mo concentrations and thus the Mo isotope ratios in the Siah-Kuh mafic enclaves got modified by a hydrothermal fluid. If such a process also affected any of the other cumulates (Adamello, California or Kos) cannot be answered with our dataset.

6. Conclusion

Here we document that arc-related magmatic cumulates represent an isotopically light Ti reservoir, counterbalancing the evolved and heavy felsic magmas. Titanium isotopic compositions of cumulates negatively correlate with increasing Fe—Ti oxide abundance, supporting previous findings that these are the main mineral phases controlling magmatic Ti isotope fractionation in mafic to intermediate magmatic systems. Cumulate rocks with low Fe—Ti oxide modes have δ^{49}Ti values similar to coexisting basalts. In these rocks, the main Ti hosts are amphibole and pyroxene. In combining these observations, we conclude that the degree to which Ti isotopes are fractionated in a magma residue after cumulate separation depends to a first order on the fraction of Ti sequestered into magmatic oxides relative to that fixed in silicate phenocrysts along the liquid line of descent.

Cumulates analyzed in this study are variably more enriched in Mo than theoretical calculations predict. Similarly, δ^{98}Mo values are on average comparable to modern arc basalts. The occurrence of cumulates deviating from modelled Mo abundance curves can be partially ascribed to mafic rejuvenation processes, retention of differently evolved melts as intercumulus phase, and fluid dominated processes. This finding suggests that the Mo concentration in oxidized arc cumulates is a valuable and sensitive proxy for secondary low degree fluid or melt contamination processes. Importantly, a light Mo isotope reservoir to counterbalance the heavy δ^{98}Mo isotope signatures of evolved rocks as identified for Ti in cumulates is not apparent for Mo. Consequently, further studies on the Mo concentration and isotopic composition of arc-derived magmatic to magmatic-hydrothermal systems are needed to better constrain the nature of the missing light Mo isotope reservoir.

References

Aarons, S.M., Reimink, J.R., Greber, N.D., Heard, A.W., Zhang, Z., Dauphas, N., 2020. Titanium isotopes constrain a magmatic transition at the Hadean-Archean boundary in the Acasta Gneiss Complex. Sci. Adv. 6 (50), eabc9959.

Aarons, S.M., Dauphas, N., Blanchard, M., Zeng, H., Nie, N.X., Johnson, A.C., Greber, N.D., Hopp, T., 2021. Clues from Ab Initio Calculations on Titanium Isotopic Fractionation in Tholeiitic and Calc-Alkaline Magma Series. ACS Earth Space Chem. 5 (9), 2466–2480.

Ahmad, Q., Wille, M., König, S., Rosca, C., Hensel, A., Pettke, T., Hermann, J., 2021. The molybdenum isotope subduction recycling conundrum: a case study from the Tongan subduction zone, Western Alps and Alpine Corsica. Chem. Geol. 576, 120231.

Anguelova, M., Fehr, M.A., Takazawa, E., Schönbächler, M., 2022. Titanium isotope heterogeneity in the Earth's mantle: a case study of the Horoman peridotite massif. Geochim. Cosmochim. Acta. 355, 356–368.

Arvin, M., Pan, Y., Dargahi, S., Malekizadeh, A., Babaei, A., 2007. Petrochemistry of the Siah-Kuh granitoid stock southwest of Kerman, Iran: implications for initiation of Neotethys subduction. J. Asian Earth Sci. 30 (3–4), 474–489.

Audétat, A., Keppler, H., 2005. Solubility of rutile in subduction zone fluids, as determined by experiments in the hydrothermal diamond anvil cell. Earth Planet. Sci. Lett. 232 (3–4), 393–402.

Audetat, A., Pettke, T., 2003. The magmatic-hydrothermal evolution of two barren granites: a melt and fluid inclusion study of the Rito del Medio and Canada Pinabete plutons in northern New Mexico (USA). Geochim. Cosmochim. Acta 67, 97–121.

Bezard, R., Fischer-Gödde, M., Hamelin, C., Brennecka, G.A., Kleine, T., 2016. The effects of magmatic processes and crustal recycling on the molybdenum stable isotopic composition of Mid-Ocean Ridge Basalts. Earth Planet. Sci. Lett. 453, 171–181.

Blundy, J.D., Sparks, R.S.J., 1992. Petrogenesis of mafic inclusions in granitoids of the Adamello Massif, Italy. J. Petrol. 33 (5), 1039–1104.

Burkhardt, C., Hin, R.C., Kleine, T., Bourdon, B., 2014. Evidence for Mo isotope fractionation in the solar nebula and during planetary differentiation. Earth Planet. Sci. Lett. 391, 201–211.

Chen, S., Hin, R.C., John, T., Brooker, R., Bryan, B., Niu, Y., Elliott, T., 2019. Molybdenum systematics of subducted crust record reactive fluid flow from underlying slab serpentine dehydration. Nat. Commun. 10 (1), 1–9.

Chen, S., Niu, Y., Gong, H., Wang, X., Xue, Q., 2022. Re-assessment of the effect of fractional crystallization on Mo isotopes: constraints from I-type granitoids and their enclosed mafic magmatic enclaves. Chem. Geol. 597, 120814.

Deng, Z., Chaussidon, M., Savage, P., Robert, F., Pik, R., Moynier, F., 2019. Titanium isotopes as a tracer for the plume or island arc affinity of felsic rocks. Proc. Natl. Acad. Sci. 116 (4), 1132–1135.

Elkins-Tanton, L.T., Burgess, S., Yin, Q.Z., 2011. The lunar magma ocean: reconciling the solidification process with lunar petrology and geochronology. Earth Planet. Sci. Lett. 304 (3–4), 326–336.

Fan, J.J., Wang, Q., Li, J., Wei, G.J., Ma, J.L., Ma, L., Zhang, L., 2021. Boron and molybdenum isotopic fractionation during crustal anatexis: constraints from the Conadong leucogranites in the Himalayan Block, South Tibet. Geochim. Cosmochim. Acta 297, 120–142.

Farges, F., Brown Jr., G.E., 1997. Coordination chemistry of titanium (IV) in silicate glasses and melts: IV. XANES studies of synthetic and natural volcanic glasses and tektites at ambient temperature and pressure. Geochim. Cosmochim. Acta 61 (9), 1863–1870.

Freymuth, H., Vils, F., Willbold, M., Taylor, R.N., Elliott, T., 2015. Molybdenum mobility and isotopic fractionation during subduction at the Mariana arc. Earth Planet. Sci. Lett. 432, 176–186.

Freymuth, H., Elliott, T., Van Soest, M., Skora, S., 2016. Tracing subducted black shales in the Lesser Antilles arc using molybdenum isotope ratios. Geology 44 (12), 987–990.

Gaschnig, R.M., Reinhard, C.T., Planavsky, N.J., Wang, X., Asael, D., Chauvel, C., 2017. The molybdenum isotope system as a tracer of slab input in subduction zones: an example from Martinique, Lesser Antilles Arc. Geochem. Geophys. Geosyst. 18 (12), 4674–4689.

Gfeller, L., 2016. Isotope Fractionation of Molybdenum during Fractional Crystallization. MSc thesis.. University of Bern.

Giere, R., 1990. Hydrothermal mobility of Ti, Zr and REE: examples from the Bergell and Adamello contact aureoles (Italy). Terra Nova 2 (1), 60–67.

Goldschmidt, V.M., 1930. Geochemische verteilungsgesetze und kosmische häufigkeit der elemente. Naturwissenschaften 18 (47), 999–1013.

Greaney, A.T., Rudnick, R.L., Gaschnig, R.M., Whalen, J.B., Luais, B., Clemens, J.D., 2018. Geochemistry of molybdenum in the continental crust. Geochim. Cosmochim. Acta 238, 36–54.

Greber, N.D., Siebert, C., Nägler, T.F., Pettke, T., 2012. δ98/95Mo values and molybdenum concentration data for NIST SRM 610, 612 and 3134: Towards a common protocol for reporting Mo data. Geostand. Geoanal. Res. 36 (3), 291–300.

Greber, N., Van Zuilen, K., 2022. Multi-collector inductively coupled plasma mass spectrometry: new developments and basic concepts for high-precision measurements of mass-dependent isotope signatures. Chimia 76 (1–2), 18.

Greber, N.D., Hofmann, B.A., Voegelin, A.R., Villa, I.M., Nägler, T.F., 2011. Mo isotope composition in Mo-rich high-and low-T hydrothermal systems from the Swiss Alps. Geochim. Cosmochim. Acta 75 (21), 6600–6609.

Greber, N.D., Pettke, T., Nägler, T.F., 2014. Magmatic–hydrothermal molybdenum isotope fractionation and its relevance to the igneous crustal signature. Lithos 190, 104–110.

Greber, N.D., Puchtel, I.S., Nägler, T.F., Mezger, K., 2015. Komatiites constrain molybdenum isotope composition of the Earth's mantle. Earth Planet. Sci. Lett. 421, 129–138.

Greber, N.D., Dauphas, N., Bekker, A., Ptáček, M.P., Bindeman, I.N., Hofmann, A., 2017a. Titanium isotopic evidence for felsic crust and plate tectonics 3.5 billion years ago. Science 357 (6357), 1271–1274.

Greber, N.D., Dauphas, N., Puchtel, I.S., Hofmann, B.A., Arndt, N.T., 2017b. Titanium stable isotopic variations in chondrites, achondrites and lunar rocks. Geochim. Cosmochim. Acta 213, 534–552.

Greber, N.D., Pettke, T., Vilela, N., Lanari, P., Dauphas, N., 2021. Titanium isotopic compositions of bulk rocks and mineral separates from the Kos magmatic suite: insights into fractional crystallization and magma mixing processes. Chem. Geol. 578, 120303.

Grove, T.L., Baker, M.B., 1984. Phase equilibrium controls on the tholeiitic versus calc-alkaline differentiation trends. J. Geophys. Res. Solid Earth 89 (B5), 3253–3274.

Grove, T.L., Kinzler, R.J., 1986. Petrogenesis of andesites. Annu. Rev. Earth Planet. Sci. 14, 417.

Hacker, B.R., Kelemen, P.B., Behn, M.D., 2015. Continental lower crust. Annu. Rev. Earth Planet. Sci. 43, 167–205.

Hess, M., 2013. What Triggered the Giant Eruption of the Kos Plateau Tuff, Greece. MSc thesis. University of Bern.

Hin, R.C., Hibbert, K.E., Chen, S., Willbold, M., Andersen, M.B., Kiseeva, E.S., Wood, B.J., Niu, Y., Sims, K.W., Elliott, T., 2022. The influence of crustal recycling on the molybdenum isotope composition of the Earth's mantle. Earth Planet. Sci. Lett. 595, 117760.

Hoare, L., Klaver, M., Saji, N.S., Gillies, J., Parkinson, I.J., Lissenberg, C.J., Millet, M.A., 2020. Melt chemistry and redox conditions control titanium isotope fractionation during magmatic differentiation. Geochim. Cosmochim. Acta 282, 38–54.

Hoare, L., Klaver, M., Muir, D.D., Klemme, S., Barling, J., Parkinson, I.J., Millet, M.A., 2022. Empirical and experimental constraints on Fe-Ti oxide-melt titanium isotope fractionation factors. Geochim. Cosmochim. Acta 326, 253–272.

Jagoutz, O., Kelemen, P.B., 2015. Role of arc processes in the formation of continental crust. Annu. Rev. Earth Planet. Sci. 43, 363–404.

Jenner, F.E., O'Neill, H.S.C., Arculus, R.J., Mavrogenes, J.A., 2010. The magnetite crisis in the evolution of arc-related magmas and the initial concentration of Au, Ag and Cu. J. Petrol. 51 (12), 2445–2464.

Kaufmann, A.K., Pettke, T., Wille, M., 2021. Molybdenum isotope fractionation at upper-crustal magmatic-hydrothermal conditions. Chem. Geol. 578, 120319.

Klaver, M., MacLennan, S.A., Ibañez-Mejia, M., Tissot, F.L., Vroon, P.Z., Millet, M.A., 2021. Reliability of detrital marine sediments as proxy for continental crust composition: The effects of hydrodynamic sorting on Ti and Zr isotope systematics. Geochim. Cosmochim. Acta. 310, 221–239.

Klaver, M., Matveev, S., Berndt, J., Lissenberg, C.J., Vroon, P.Z., 2017. A mineral and cumulate perspective to magma differentiation at Nisyros volcano, Aegean arc. Contrib. Mineral. Petrol. 172 (11), 1–23.

Klemme, S., Günther, D., Hametner, K., Prowatke, S., Zack, T., 2006. The partitioning of trace elements between ilmenite, ulvospinel, armalcolite and silicate melts with implications for the early differentiation of the moon. Chem. Geol. 234 (3–4), 251–263.

König, S., Wille, M., Voegelin, A., Schoenberg, R., 2016. Molybdenum isotope systematics in subduction zones. Earth Planet. Sci. Lett. 447, 95–102.

Krättli, G., Schmidt, M.W., 2021. Experimental settling, floatation and compaction of plagioclase in basaltic melt and a revision of melt density. Contrib. Mineral. Petrol. 176 (4), 1–27.

Lee, C.-T.A., Morton, D.M., Farner, M.J., Moitra, P., 2015. Field and model constraints on silicic melt segregation by compaction/hindered settling: the role of water and its effect on latent heat release. Am. Mineral. 100 (8–9), 1762–1777. https://doi.org/10.2138/am-2015-5121.

Leitzke, F.P., Fonseca, R.O., Sprung, P., Mallmann, G., Lagos, M., Michely, L.T., Münker, C., 2017. Redox dependent behaviour of molybdenum during magmatic processes in the terrestrial and lunar mantle: implications for the Mo/W of the bulk silicate Moon. Earth Planet. Sci. Lett. 474, 503–515.

Leitzke, F.P., Fonseca, R.O.C., Göttlicher, J., Steininger, R., Jahn, S., Prescher, C., Lagos, M., 2018. Ti K-edge XANES study on the coordination number and oxidation state of titanium in pyroxene, olivine, armalcolite, ilmenite, and silicate glass during mare basalt petrogenesis. Contrib. Mineral. Petrol. 173 (12), 1–17.

Li, Y., McCoy-West, A.J., Zhang, S., Selby, D., Burton, K.W., Horan, K., 2019. Controlling mechanisms for molybdenum isotope fractionation in porphyry deposits: the Qulong example. Econ. Geol. 114 (5), 981–992.

Li, H.Y., Zhao, R.P., Li, J., Tamura, Y., Spencer, C., Stern, R.J., Xu, Y.G., 2021. Molybdenum isotopes unmask slab dehydration and melting beneath the Mariana arc. Nat. Commun. 12 (1), 1–10.

Lodders, K., Palme, H., 1991. On the chalcophile character of molybdenum: determination of sulphide/silicate partition coefficients of Mo and W. Earth Planet. Sci. Lett. 103 (1–4), 311–324.

Ma, L., Xu, Y.G., Li, J., Chen, L.H., Liu, J.Q., Li, H.Y., Wang, Y., 2022. Molybdenum isotopic constraints on the origin of EM1-type continental intraplate basalts. Geochim. Cosmochim. Acta 317, 255–268.

Mandl, M.B., 2019. Titanium Isotope Fractionation on the Earth and Moon: Constraints on Magmatic Processes and Moon Formation. Doctoral dissertation,. ETH Zurich.

Marxer, F., Ulmer, P., Müntener, O., 2022. Polybaric fractional crystallisation of arc magmas: an experimental study simulating trans-crustal magmatic systems. Contrib. Mineral. Petrol. 177 (1), 1–36.

McCoy-West, A.J., Chowdhury, P., Burton, K.W., Sossi, P., Nowell, G.M., Fitton, J.G., Williams, H.M., 2019. Extensive crustal extraction in Earth's early history inferred from molybdenum isotopes. Nat. Geosci. 12 (11), 946–951.

Millet, M.A., Dauphas, N., 2014. Ultra-precise titanium stable isotope measurements by double-spike high resolution MC-ICP-MS. J. Anal. At. Spectrom. 29 (8), 1444–1458.

Millet, M.A., Dauphas, N., Greber, N.D., Burton, K.W., Dale, C.W., Debret, B., Williams, H.M., 2016. Titanium stable isotope investigation of magmatic processes on the Earth and Moon. Earth Planet. Sci. Lett. 449, 197–205.

Müntener, O., Ulmer, P., 2018. Arc crust formation and differentiation constrained by experimental petrology. Am. J. Sci. 318 (1), 64–89.

Mysen, B.O., Ryerson, F.J., Virgo, D., 1980. The influence of TiO2 on the structure and derivative properties of silicate melts. Am. Mineral. 65 (11–12), 1150–1165.

Nandedkar, R.H., Ulmer, P., Müntener, O., 2014. Fractional crystallization of primitive, hydrous arc magmas: an experimental study at 0.7 GPa. Contrib. Mineral. Petrol. 167 (6), 1–27.

Nebel-Jacobsen, Y., Wille, M., Ivanic, T., Nebel, O., 2021. Molybdenum isotope systematics in cumulate rock of the 2.8 Windimurra layered intrusion: A test for igneous differentiation and the composition of the Archean mantle. Precambrian Res. 355, 106087.

Neely, R.A., Gislason, S.R., Ólafsson, M., McCoy-West, A.J., Pearce, C.R., Burton, K.W., 2018. Molybdenum isotope behaviour in groundwaters and terrestrial hydrothermal systems, Iceland. Earth Planet. Sci. Lett. 486, 108–118.

Neubert, N., Heri, A.R., Voegelin, A.R., Nägler, T.F., Schlunegger, F., Villa, I.M., 2011. The molybdenum isotopic composition in river water: constraints from small catchments. Earth Planet. Sci. Lett. 304 (1–2), 180–190.

Newsom, Horton E., Palme, Herbert, 1984. The depletion of siderophile elements in the Earth's mantle: new evidence from molybdenum and tungsten. Earth Planet. Sci. Lett. 69 (3), 354–364.

Nie, N.X., Dauphas, N., Alp, E.E., Zeng, H., Sio, C.K., Hu, J.Y., Chen, X., Aarons, S.M., Zhang, Z., Tian, H.C., Wang, D., 2021. Iron, magnesium, and titanium isotopic fractionations between garnet, ilmenite, fayalite, biotite, and tourmaline: results from NRIXS, ab initio, and study of mineral separates from the Moosilauke metapelite. Geochim. Cosmochim. Acta 302, 18–45.

Nimis, P., Ulmer, P., 1998. Clinopyroxene geobarometry of magmatic rocks part 1: an expanded structural geobarometer for anhydrous and hydrous, basic and ultrabasic systems. Contrib. Mineral. Petrol. 133 (1), 122–135.

Pearce, J.A., Norry, M.J., 1979. Petrogenetic implications of Ti, Zr, Y, and Nb variations in volcanic rocks. Contrib. Mineral. Petrol. 69 (1), 33–47.

Peters, D., Pettke, T., 2017. Evaluation of major to ultra trace element bulk rock chemical analysis of nanoparticulate pressed powder pellets by LA-ICP-MS. Geostand. Geoanal. Res. 41 (1), 5–28.

Rapp, J.F., Klemme, S., Butler, I.B., Harley, S.L., 2010. Extremely high solubility of rutile in chloride and fluoride-bearing metamorphic fluids: an experimental investigation. Geology 38 (4), 323–326.

Reubi, O., Blundy, J., 2008. Assimilation of plutonic roots, formation of high-K 'exotic' melt inclusions and genesis of andesitic magmas at Volcán de Colima, Mexico. J. Petrol. 49 (12), 2221–2243.

Righter, K., Danielson, L.R., Pando, K.M., Shofner, G.A., Sutton, S.R., Newville, M., Lee, C.T., 2016. Valence and metal/silicate partitioning of Mo: Implications for conditions of Earth accretion and core formation. Earth Planet. Sci. Lett. 437, 89–100.

Rudge, J.F., Reynolds, B.C., Bourdon, B., 2009. The double spike toolbox. Chem. Geol. 265 (3–4), 420–431.

Rudnick, R.L., 1995. Making continental crust. Nature 378 (6557), 571–578.

Rzehak, L.J., Kommescher, S., Kurzweil, F., Sprung, P., Leitzke, F.P., Fonseca, R.O., 2021. The redox dependence of titanium isotope fractionation in synthetic Ti-rich lunar melts. Contrib. Mineral. Petrol. 176 (3), 1–16.

Rzehak, L.J.A., Kommescher, S., Hoare, L., Kurzweil, F., Sprung, P., Leitzke, F., Fonseca, R., 2022. Redox-dependent Ti stable isotope fractionation on the Moon: implications for current lunar magma ocean models. Contrib. Mineral. Petrol. 177, 81 (2022). https://doi.org/10.1007/s00410-022-01947-0.

Schneider, C.A., Rasband, W.S., Eliceiri, K.W., 2012. NIH image to ImageJ: 25 years of image analysis. Nat. Methods 9 (7), 671–675.

Schuessler, J.A., Schoenberg, R., Sigmarsson, O., 2009. Iron and lithium isotope systematics of the Hekla volcano, Iceland—evidence for Fe isotope fractionation during magma differentiation. Chem. Geol. 258 (1–2), 78–91.

Shafiei, B., Shamanian, G., Mathur, R., Mirnejad, H., 2015. Mo isotope fractionation during hydrothermal evolution of porphyry Cu systems. Mineral. Deposita 50 (3), 281–291.

Shervais, J.W., 1982. Ti-V plots and the petrogenesis of modern and ophiolitic lavas. Earth Planet. Sci. Lett. 59 (1), 101–118.

Sievwright, R.H., O'Neill, H.S.C., Tolley, J., Wilkinson, J.J., Berry, A.J., 2020. Diffusion and partition coefficients of minor and trace elements in magnetite as a function of oxygen fugacity at 1150 °C. Contrib. Mineral. Petrol. 175 (5), 1–21.

Sisson, T.W., Grove, T.L., Coleman, D.S., 1996. Hornblende gabbro sill complex at Onion Valley, California, and a mixing origin for the Sierra Nevada batholith. Contrib. Mineral. Petrol. 126 (1–2), 81–108.

Storck, J.C., Wotzlaw, J.F., Karakas, Ö., Brack, P., Gerdes, A., Ulmer, P., 2020. Hafnium isotopic record of mantle-crust interaction in an evolving continental magmatic system. Earth Planet. Sci. Lett. 535, 116100.

Storck, J.C., Laurent, O., Karakas, O., Wotzlaw, J.F., Galli, A., Sinigoi, S., Chelle-Michou, C., 2021. Mantle versus crustal contributions in crustal-scale magmatic systems (Sesia Magmatic System, northern Italy) from coupling Hf isotopes and numerical modelling. Contrib. Mineral. Petrol. 176 (11), 1–19.

Tattitch, B.C., Blundy, J.D., 2017. Cu-Mo partitioning between felsic melts and saline-aqueous fluids as a function of X-NaCleq, f(O2), and f(S2). Am. Mineral. 102, 1987–2006.

Taylor, S.R., White, A.J.R., 1965. Geochemistry of andesites and the growth of continents. Nature 208 (5007), 271–273.

Teng, F.Z., Dauphas, N., Helz, R.T., 2008. Iron isotope fractionation during magmatic differentiation in Kilauea Iki lava lake. Science 320 (5883), 1620–1622.

Tiepolo, M., Tribuzio, R., Vannucci, R., 2002. The compositions of mantle-derived melts developed during the Alpine continental collision. Contrib. Mineral. Petrol. 144 (1), 1–15.

Tiepolo, M., Tribuzio, R., Langone, A., 2011. High-Mg andesite petrogenesis by amphibole crystallization and ultramafic crust assimilation: evidence from Adamello hornblendites (Central Alps, Italy). J. Petrol. 52 (5), 1011–1045.

Tropper, P., Manning, C.E., 2005. Very low solubility of rutile in H2O at high pressure and temperature, and its implications for Ti mobility in subduction zones. Am. Mineral. 90 (2–3), 502–505.

Ulmer, P., Callegari, E., Sonderegger, U.C., 1983. Genesis of the mafic and ultramafic rocks and their genetical relations to the tonalitic-trondhjemitic granitoids of the southern part of the Adamello batholith (Northern Italy). Mem. Soc. Geol. Ital. 26 (1), 171–222.

Vieira Duarte, J.F., Piccoli, F., Pettke, T., Hermann, J., 2021. Textural and geochemical evidence for magnetite production upon antigorite breakdown during subduction. J. Petrol. 62, 1–29.

Villalobos-Orchard, J., Freymuth, H., O'Driscoll, B., Elliott, T., Williams, H., Casalini, M., Willbold, M., 2020. Molybdenum isotope ratios in Izu arc basalts: the control of subduction zone fluids on compositional variations in arc volcanic systems. Geochim. Cosmochim. Acta 288, 68–82.

Villiger, S., Ulmer, P., Müntener, O., 2007. Equilibrium and fractional crystallization experiments at 0· 7 GPa; the effect of pressure on phase relations and liquid compositions of tholeiitic magmas. J. Petrol. 48 (1), 159–184.

Voegelin, A.R., Nägler, T.F., Pettke, T., Neubert, N., Steinmann, M., Pourret, O., Villa, I. M., 2012. The impact of igneous bedrock weathering on the Mo isotopic composition of stream waters: natural samples and laboratory experiments. Geochim. Cosmochim. Acta 86, 150–165.

Voegelin, A.R., Pettke, T., Greber, N.D., von Niederhäusern, B., Nägler, T.F., 2014. Magma differentiation fractionates Mo isotope ratios: evidence from the Kos Plateau Tuff (Aegean Arc). Lithos 190, 440–448.

Wang, Z., Becker, H., 2018. Molybdenum partitioning behavior and content in the depleted mantle: insights from Balmuccia and Baldissero mantle tectonites (Ivrea Zone, Italian Alps). Chem. Geol. 499, 138–150.

Wang, W., Huang, S., Huang, F., Zhao, X., Wu, Z., 2020. Equilibrium inter-mineral titanium isotope fractionation: implication for high-temperature titanium isotope geochemistry. Geochim. Cosmochim. Acta 269, 540–553.

Wijbrans, C.H., Klemme, S., Berndt, J., Vollmer, C., 2015. Experimental determination of trace element partition coefficients between spinel and silicate melt: the influence of chemical composition and oxygen fugacity. Contrib. Mineral. Petrol. 169 (4), 1–33.

Willbold, M., Hibbert, K., Lai, Y.J., Freymuth, H., Hin, R.C., Coath, C., Elliott, T., 2016. High-precision mass-dependent Molybdenum isotope variations in magmatic rocks determined by double-spike MC-ICP-MS. Geostand. Geoanal. Res. 40 (3), 389–403.

Wille, M., Nebel, O., Van Kranendonk, M.J., Schoenberg, R., Kleinhanns, I.C., Ellwood, M.J., 2013. Mo–Cr isotope evidence for a reducing Archean atmosphere in 3.46–2.76 Ga black shales from the Pilbara, Western Australia. Chem. Geol. 340, 68–76.

Wille, M., Nebel, O., Pettke, T., Vroon, P.Z., König, S., Schoenberg, R., 2018. Molybdenum isotope variations in calc-alkaline lavas from the Banda arc, Indonesia: assessing the effect of crystal fractionation in creating isotopically heavy continental crust. Chem. Geol. 485, 1–13.

Williams, N.H., Fehr, M.A., Parkinson, I.J., Mandl, M.B., Schönbächler, M., 2021. Titanium isotope fractionation in solar system materials. Chem. Geol. 568, 120009.

Yang, J., Barling, J., Siebert, C., Fietzke, J., Stephens, E., Halliday, A.N., 2017. The molybdenum isotopic compositions of I-, S-and A-type granitic suites. Geochim. Cosmochim. Acta 205, 168–186.

Young, E.D., Manning, C.E., Schauble, E.A., Shahar, A., Macris, C.A., Lazar, C., Jordan, M., 2015. High-temperature equilibrium isotope fractionation of non-traditional stable isotopes: experiments, theory, and applications. Chem. Geol. 395, 176–195.

Yu, Y., Huang, X.L., Chung, S.L., Li, J., Lai, Y.M., Setiawan, I., Sun, M., 2022. Molybdenum isotopic constraint from Java on slab inputs to subduction zone magmatism. Geochim. Cosmochim. Acta 332, 1–18.

Zajacz, Z., Halter, W.E., Pettke, T., Guillong, M., 2008. Determination of fluid/melt partition coefficients by LA-ICPMS analysis of co-existing fluid and silicate melt inclusions: controls on element partitioning. Geochim. Cosmochim. Acta 72 (8), 2169–2197.

Zhang, J., Dauphas, N., Davis, A.M., Pourmand, A., 2011. A new method for MC-ICPMS measurement of titanium isotopic composition: Identification of correlated isotope anomalies in meteorites. J. Anal. At. Spectrom. 26 (11), 2197–2205.

Zhao, X., Tang, S., Li, J., Wang, H., Helz, R., Marsh, B., Zhang, H., 2020. Titanium isotopic fractionation during magmatic differentiation. Contrib. Mineral. Petrol. 175 (7), 1–16.